Interrogation of cancer gene dependencies reveals novel paralog interactions of autosome and sex chromosome encoded genes

Anna Köferle[1,*], Andreas Schlattl[1,*], Alexandra Hörmann[1], Fiona Spreitzer[1], Alexandra Popa[1], Venu Thatikonda[1], Teresa Puchner[1], Sarah Oberndorfer[1], Corinna Wieshofer[1], Maja Corcokovic[1], Christoph Reiser[1], Simon Wöhrle[1], Johannes Popow[1], Mark Pearson[1], Barbara Mair[1,$], Ralph A. Neumüller[1,$]

[1] Boehringer Ingelheim RCV GmbH & Co KG, Doktor-Boehringer-Gasse 5-11, 1120, Vienna, Austria
* Equal contributing first authors
[$] Equal contributing last authors
[$] to whom correspondence should be addressed: barbara.mair@boehringer-ingelheim.com, ralph.neumueller@boehringer-ingelheim.com,

Abstract

Genetic networks are characterized by extensive buffering. During tumour evolution, disruption of these functional redundancies can create *de novo* vulnerabilities that are specific to cancer cells. In this regard, paralog genes are of particular interest, as the loss of one paralog gene can render tumour cells dependent on a remaining paralog. To systematically identify cancer-relevant paralog dependencies, we searched for candidate dependencies using CRISPR screens and publicly available loss-of-function datasets. Our analysis revealed >2,000 potential candidate dependencies, several of which were subsequently experimentally validated. We provide evidence that *DNAJC15-DNAJC19*, *FAM50A-FAM50B* and *RPP25-RPP25L* are novel cancer relevant paralog dependencies. Importantly, our analysis also revealed unexpected redundancies between sex chromosome genes. We show that chrX- and chrY-encoded paralogs, as exemplified by *ZFX-ZFY*, *DDX3X-DDX3Y* and *EIF1AX-EIF1AY*, are functionally linked so that tumour cell lines from male patients with Y-chromosome loss become exquisitely dependent on the chrX-encoded gene. We therefore propose genetic redundancies between chrX- and chrY- encoded paralogs as a general therapeutic strategy for human tumours that have lost the Y-chromosome.

Introduction

Paralog genes that fulfill similar functions provides a degree of robustness of gene regulatory networks to deleterious events[1–3]. These paralog genes arise as a result of gene duplications and subsequent divergent evolution[4,5]. Paralog redundancies are of interest to cancer biology, as tumour-specific processes like hypermethylation, mutations or copy number alterations can inactivate genes and thereby reduce the extent of genetic buffering. Genes whose loss is buffered in non-neoplastic cells by a paralog can thus become dependencies in tumours where the redundant paralog is absent. Examples for such paralog dependencies in cancer cells have been identified and validated before, and include *ENO1-ENO2*[6], *SMARCA2-SMARCA4*[7–9], *ARID1A-ARID1B*[10] or *STAG1-STAG2*[11,12].

In all validated cases, the tumour-specific loss of one paralog gene creates a specific dependency on a remaining paralog. Accordingly, therapeutic inhibition of the remaining paralog gene is assumed to be safe, because non-tumour cells still retain the genetic buffer to tolerate the inhibition without systemic side effects. Another advantage of tumour-specific vulnerabilities created by loss of a paralogous gene is the availability of a tractable biomarker; i.e. measuring loss of Paralog A in tumours allows to select patients that would respond to inhibition of the synthetic lethal Paralog B. Therefore, paralog dependencies represent a highly attractive concept for cancer drug target identification. However, a systematic understanding of cancer-relevant paralog dependencies is still elusive to date, although CRISPR-based combinatorial screens and bioinformatics discovery pipelines are beginning to shed light on the tumour redundancy map[3,13–20].

In addition to mutagenic processes such as gene silencing, point mutations or gene amplification, human cancers frequently lose large amounts of their genetic material during the process of tumourigenesis[21]. Deletions can involve one or multiple genes or, as is being appreciated, extend to loss of whole chromosomes, one of the most prevalent being loss of chromosome Y (LOY). Cancer incidence is generally higher in males[22,23], a fact that has been attributed to the general protective effect of the chrXX status in females that allows buffering of deleterious mutations[24,25]. LOY has been reported in ~93% of esophageal adenocarcinomas[26], ~12% of male breast cancers[27] and ~23% of urothelial bladder cancer samples[28]. Mosaic loss of chrY has also been observed outside of the oncology context, where it has been correlated with increased age[29–31]. LOY has been associated with a number of pathophysiological conditions, including clonal hematopoiesis and Alzheimer's disease[32,33]. Due to the plethora of disease states in which LOY occurs, strategies to eliminate cells involved in pathological conditions, including neoplastic transformation is clearly of general medical interest.

We set out to discover cancer-relevant paralog dependencies by an integrative approach of combining multiple -omics datasets in panels of human cancer cell lines. This analysis reveals 2,040 candidate paralog gene interactions, a subset of which we validate experimentally. Importantly, we uncover a sex-chromosome-specific set of genes that is functionally buffered between the X and Y chromosomes. We demonstrate that targeted depletion of the chrX-encoded gene in LOY tumour cell lines offers an attractive strategy to treat tumours that have lost chrY. In addition, these results provide a generalizable framework of how to eliminate putative pre-pathogenic LOY cells.

Results

CRISPR/Cas9 screens identify *CSTF2-CSTF2T* as a paralog dependency

We devised a set of proof-of-principle CRISPR screens to investigate the concept of cancer-specific paralog dependencies. We started by cataloging potential human paralog genes from Ensembl BioMarT, as defined by all genes with at least one other paralog in the same family without any further constraints on homology or family size. Most of the multi-gene families contain two to five paralog genes and the biggest class of genes are protein-coding genes (Figure 1a,b). A compact protein domain-focused CRISPR gRNA library[34] of ~10,000 gRNAs was generated to permit screening across multiple tumour cell lines. The library genes were manually curated to contain genes that are frequently deleted

76 in human solid tumours, including 460 unique paralog genes from 199 families. Loss-Of-Function (LOF)
77 screens were then carried out across seven cancer cell lines (Hep 3B2.1-7, HuP-T4, MIA PaCa-2, NCI-
78 H1373, NCI-H1993, NCI-H2009, PC-9) with annotated deep deletions (see Methods).

79 Paralog genes scoring as significantly depleted in our screens were cross-referenced across the different
80 cell lines to understand whether any of their family members were annotated as deleted (Figure 1c,
81 Supplementary Table 1). Accordingly, we found that *ATP4B* was specifically required in Hep 3B2.1-7 cells
82 that harbor a deletion of *ATP1B2*. Both genes are subunits of potassium-transporting ATPases, but
83 physical or functional interactions have not been described. Furthermore, we observed that NCI-H1993
84 cells were particularly sensitive to loss of *CSTF2*, likely due to a deletion of its paralog *CSTF2T*. *CSTF2* and
85 *CSTF2T* encode the CstF-64 and CstF-64tau proteins respectively, that have partially overlapping
86 functions in the Cleavage stimulation Factor (CstF) complex, a regulatory component of the mRNA
87 cleavage and polyadenylation machinery[35–37]. We confirmed the sensitivity of *CSTF2T*-negative cells to
88 depletion of *CSTF2* (Figure 1d, Supplementary Figure 1). Mechanistically, we observed that depletion of
89 *CSTF2* leads to compensatory induction of *CSTF2T* in *CSTF2T*-proficient cells (Figure 1e), confirming
90 previous reports describing that *CSTF2* and *CSTF2T* can regulate each other's expression[36–38]. This
91 compensatory upregulation is not observed in *CSTF2T*-deficient cell lines (Figure 2f), providing a
92 hypothesis for the dependency on *CSTF2*. Of note, *CSTF2* and *CSTF2T* are encoded by a single essential
93 gene in yeast, *RNA15* (*YGL044C*)[39], suggesting that cellular viability might depend on the activity of both
94 paralogues in mice and humans. In mice, previous studies suggest that *Cstf2* and *Cstf2t* form a
95 functionally redundant pair of genes with an essential function in certain contexts. Embryonic stem cells
96 lacking *Cstf2* had altered pluripotency and could be differentiated into mesoderm and ectoderm, but
97 not endoderm[38,40]. Autosomally encoded *CSTF2T* is required in pachytene spermatocytes to overcome
98 the lack of expression of X-encoded *CSTF2* due to meiotic sex chromosome inactivation, leading to male
99 sterility[35]. Hence, some but not all functions of Cstf2 can be assumed by Cstf2t.

100 In summary, this set of proof-of-concept screens - despite their limited scope - demonstrates that *bona*
101 *fide* paralog dependencies are detectable using pooled LOF screens in cancer cell lines.

102

103 **Bioinformatic identification of cancer-relevant candidate paralog dependencies**

104 Due to the limited search space and number of paralog dependencies retrieved from our focused
105 experimental approach, we decided to search for candidate interactions in a systematic manner,
106 leveraging publicly available LOF and expression data from hundreds of cancer cell lines. We
107 hypothesized that candidate genetic interactions between paralogous genes could be detected by
108 looking at the relationship between expression of Paralog A and dependency on Paralog B. In essence, if
109 low expression of Paralog A ("biomarker") was correlated with sensitivity to loss of Paralog B ("query"),
110 this would identify a potential genetic interaction that could subsequently be evaluated. Depletion
111 scores from complementary datasets[41] of pooled CRISPR and shRNA screens (AVANA[42], Sanger[43] and
112 DRIVE[44]) and corresponding gene and protein expression data[45,46] for paralog genes were collected.
113 Correlation coefficients and corresponding p-values between expression levels of biomarkers and
114 depletion scores of queries for as many pairs within each paralog family where expression/depletion
115 data were available were then calculated. This approach resulted in a large matrix of correlation tests,

116 containing 14,064 unique genes (biomarkers or queries) and 108,092 unique biomarker-query pairs
117 (Supplementary Table 2), hereafter called PaCT (Paralog Cancer Targets). The obtained correlation
118 coefficients was then filtered via a cutoff of 3*SD (standard deviation) and p-value < 0.05 to generate a
119 hit set (Figure 2a,b; Supplementary Table 2). Simulating the distribution of Spearman correlation
120 coefficients by randomly assigning each query to a gene from different family yields very few
121 interactions at similarly strong correlations, indicating the specificity of PaCT candidate pairs (see
122 Methods; Figure 2c).

123 In contrast to other recent paralog studies, we did not limit the PaCT search space to paralog pairs by a
124 similarity cutoff or membership in a paralog gene family of a given (small) size[13,19]. An additional
125 advantage of PaCT is the ability to identify candidate interaction partners for genes that have not been
126 targeted themselves as queries, as long as expression data are available for them to act as biomarkers.
127 Overall, of 3,084,147 possible pairs (including self-interactions) from 3,587 paralogue families, PaCT is
128 blind to 2,975,741 pairs (2,795 genes), due to missing depletion and/or expression data for either query
129 or biomarker or both. This also includes pairs where information is available only for a single cell line and,
130 therefore, where no correlation can be calculated. From the remaining 108,406 paralogue pairs, 2,040
131 unique pairs (1.9%) were identified as significant interactions, and for 106,366 paralogue pairs (98.1%;
132 14,055 genes), we identified a non-significant correlation in our analysis (Figure 2d).

133 We then sought to identify possible differences between hit and non-hit paralogue pairs. Insufficient
134 variability in gene/protein expression and/or depletion scores across the cell lines could underlie low
135 correlation coefficients across our dataset. We investigated this for gene expression levels and depletion
136 scores from the AVANA dataset as an example. Indeed, we identified a small, but statistically significant
137 difference in variabilities for both modalities (p-value < 2.2×10^{-16}, Kolmogorov-Smirnov test) between
138 hits and non-hits (Figure 2e,f). We further hypothesized that sequence similarity between individual
139 paralog genes could impact the likelihood for an interaction between them. Indeed, based on Ensembl
140 BioMarT DNA sequence similarity, we observed a significant trend that genes involved in significant
141 paralog interactions exhibit higher similarity than those of non-significant pairs (Figure 2g).

142 Interestingly, significant pairwise candidate interactions are observed between paralogs in families of
143 any size (Figure 2h). Even though many candidate pairs are interactions within 2-member paralog
144 families, we scored significant correlations in larger families of up to 20 members or more. In smaller
145 families, the majority are positive correlations; with increasing family size, the balance shifts towards an
146 even split with negative correlations. On average (AVANA data), we identified 8.4% significant
147 interactions per family when family size is <= 10 that decreased to 1.4% for families containing more
148 than 10 genes (Figure 2i, Supplementary Figure 2 a,b). Finally, we looked at connectivity within paralog
149 families and observed that this varies widely (Figure 2j,k, Supplementary Figure 2c-f). Among the hit
150 pairs, some queries and biomarkers act as hubs, being involved in multiple or all significant interactions,
151 independent of family size. However, other candidates have a more uniform distribution, being
152 identified in only a subset of hit pairs. It remains to be determined what factors underlie these different
153 degrees of connectivity.

154 As previously described by others[18,47], some gRNAs in the Sanger and AVANA datasets are promiscuous
155 and match to sites beyond the intended target. For PaCT, we used processed AVANA and Sanger scores
156 [42,43] and we confirmed (for the AVANA data as an example) that most genes had zero or one gRNA
157 excluded from the analysis for reasons identified by the investigators of the study (Supplementary

158 Figure 2g; Supplementary Table 2). However, we confirmed previous observations that a sizeable
159 fraction of query genes (25%) had non-uniquely mapping gRNAs assigned to them (Supplementary
160 Figure 2h; Supplementary Table 2), constituting a potential source of false negatives [18,47] in our analysis.

161 Of the 2,472 candidate hit query-biomarker pairs (2,040 of which are non-redundant, involving 2,451
162 unique genes), 57% displayed a positive correlation between query dependency score and biomarker
163 expression. Most pairs (70%) were found using gene expression data, reflecting the greater robustness
164 of this dataset. We also included genes whose genetic dependency correlates with their own expression,
165 and 20% of our hits are indeed such "self-pairs". 20 of them have been previously described as CYCLOPS
166 (*c*opy number alterations *y*ielding *c*ancer *l*iabilities *o*wing to *p*artial loss) genes[48,49] that, when expressed
167 at low levels, are associated with greater sensitivity to further LOF. Similar to previous observations[49],
168 CYCLOPS genes are overrepresented among the significant hits identified by PaCT (20%), compared to
169 their representation among all potential interactions (13%), mirroring the high frequency of genomic
170 loss in cancer cell lines. In total, our PaCT analysis highlighted 370 unique candidate self-interactions.

171 The largest proportion of candidate hit query-biomarker pairs (46%) was detected in the AVANA dataset
172 – representing the largest and most comprehensive database in terms of cell lines included -, followed
173 by Sanger (37%) and DRIVE (17%). The covered cell lines and genes overlap to a certain extent, but each
174 dataset contains unique cell lines and genes, in addition to differences in methodologies for generating
175 LOF phenotypes (RNAi in DRIVE vs. CRISPR in AVANA and Sanger)[41]. Thus, it is not surprising that many
176 hits are found uniquely within one dataset or data domain (gene or protein expression; Figure 3a).
177 Nevertheless, 17% (432/2,472) of candidate pairs are recovered more than once, strengthening our
178 confidence in the PaCT approach. The largest overlap was observed between AVANA and Sanger
179 positive correlations pairs using gene expression as a biomarker, confirming those as high-quality
180 candidates. To illustrate the PaCT approach, Figure 3b shows examples of strong negative or positive
181 correlations within small paralog families along the diagonal, i.e. between expression and depletion of
182 the same gene or closely related paralogs, which are listed next to each other.

183 We complemented the PaCT approach by an additional analysis of the AVANA, DRIVE and Sanger data.
184 First, we classified cell lines as sensitive and resistant to depletion of a given query gene by k-means
185 clustering (k=3, leaving out the intermediate group). Then, we tested whether the expression of a given
186 biomarker gene was significantly different between the sensitive and resistant cluster. The most significant
187 negative correlation hits are almost exclusively self-interactions (Supplementary Figure 3a-c), consistent
188 with the notion of increased sensitivity to loss of highly expressed genes that might act as proliferation
189 drivers. On the other hand, the most significant positive correlation hits are pairs of paralogs
190 (Supplementary Figure 3a-c), supporting the hypothesis of functional redundancy and synthetic lethality
191 between those genes. Overall, the PaCT top hits also emerged as most significant in this analysis.

192 In order to characterize the PaCT hits, we investigated gene-centric parameters of the candidate pairs
193 (without self-interactions) that have been hypothesized by us and others to affect the likelihood of
194 genetic interaction between paralog genes[13,18]. We observed that some of our candidate interacting
195 paralog pairs (13%) are involved in protein-protein interactions (PPI) with each other, as annotated in
196 BIOGRID[50] (v4.3.196; Supplementary Figure 3d). We then checked the candidate pairs for homo- and
197 heteromeric interactions[3], where homomeric means the assembly of a protein with itself whereas
198 heteromeric paralogs assemble with each other. None of the candidate pairs is found on the (short) list

199 of heteromers, and ~3% of queries or biomarkers are annotated as homomers (Supplementary Figure
200 3d). We also compared our list of candidate pairs to the Critical Paralog Groups (CPGs) defined by
201 Modos et al.[51], i.e. paralog groups that play important roles in signaling flow and pathway cross-talk. ~2%
202 of PaCT pairs and 4-6% of query or biomarker genes are annotated as members of CPGs (Supplementary
203 Figure 3d). Finally, we investigated whether the candidate interacting pairs share the same common
204 ortholog and whether that ortholog is essential in different model organisms (Supplementary Figure 3e).
205 While these numbers provide a mere estimate, due to the caveats of ambiguous and incomplete
206 ortholog mapping, we expected and observed increasing fractions of common essential orthologs with
207 increasing evolutionary distance – from 0.4% in *M. musculus* to >5.5% in *S. cerevisiae*. Accordingly, the
208 fraction of orthologs that could not be mapped also increased, while the fraction of non-shared
209 orthologs decreased.

210 Together, these characteristics of shared evolutionary origin and essentiality, or physical interaction,
211 describe some but not all parameters that underlie potential genetic and functional interaction between
212 paralogous genes. Recently, several groups have investigated paralog redundancy and interaction using
213 various computational and experimental methods[13–20]. We compared our PaCT candidates with their
214 sets of potentially interacting paralogs and recovered 12-67% of published pairs in our hit list
215 (Supplementary Figure 3f). Conversely, 15% of PaCT pairs are found in any other dataset. The published
216 sets originate from vastly different search spaces – from a few hundred experimentally tested pairs to
217 computational predictions of the complete interaction matrix of all annotated paralogs. Therefore, the
218 variation in recovery is not surprising and consistent with comparisons between the published
219 datasets[13–20].

220 In addition, PaCT also identified several paralog dependencies that have recently been described,
221 including *SMARCA2-SMARCA4* or *SLC25A28-SLC25A37*[19]. We used CRISPR GFP-depletion assays to
222 experimentally validate the genetic dependencies on *FAM50A* in cells where *FAM50B* expression is low,
223 and on *VPS4A* in *VPS4B*-low cell lines (Figure 3c,d and Supplementary Figure 3g,h), two paralog
224 interactions that have recently been functionally characterized[19,52,53].

225 While most hits from dual-LOF screens and experimentally validated paralog dependencies rely on the
226 absence of Paralog A to detect dependency on Paralog B (or partial loss in a CYCLOPS interaction), PaCT
227 in principle identifies candidate interactions at any level of expression. To illustrate this, we calculated
228 the fraction of hit pairs with a relevant query depletion (AVANA or Sanger score < -0.5 or DRIVE score < -
229 3) in at least one cell line when the biomarker expression is low, medium or high (Supplementary Figure
230 3i). Indeed, the theoretical validation rate of candidate interactions is ~60% for all expression bins.

231 Overall, these findings validate PaCT as a complementary approach to retrieve validated as well as novel
232 candidates for interactions between paralog genes.

233

234 **_RPP25-RPP25L_ and _DNAJC15-DNAJC19_ are novel cancer-relevant paralog interactions**

235 In addition to previously described paralog interactions, we discovered several novel high-confidence
236 candidate dependencies, among them *RPP25-RPP25L*. RPP25 has been described as a component of the

237 RNase P and RNAse MRP ribonuclease complexes that process pre-tRNA and pre-rRNA sequences,
238 respectively[54–57]. Little is known about RPP25L, a role in tRNA or rRNA processing has not been
239 functionally validated. Sensitivity to loss of *RPP25L* was observed to be correlated with low expression of
240 *RPP25* (Figure 4a, Supplementary Figure 4a,b). This was then experimentally validated using CRISPR
241 depletion assays. No depletion of *RPP25L*-targeting gRNAs was observed in cell lines that express *RPP25*
242 (Figure 4b,c). Overexpression of either *RPP25* or *RPP25L* in the sensitive U-2OS and KYSE-150 fully
243 rescued sensitivity to *RPP25L* LOF, demonstrating functional redundancy between these two paralogs
244 (Figure 4d, Supplementary Figure 4c). Interestingly, we observed a reduction in levels of endogenous
245 RPP25L upon ectopic overexpression of RPP25 (Supplementary Figure 4d,e) suggesting the existence of
246 feedback mechanisms that regulate the levels of RPP25L in response to changes in the abundance of its
247 paralog protein. In order to elucidate the underlying molecular mechanism of this paralog interaction,
248 further investigation of their role in pre-tRNA and pre-rRNA processing will be required.

249 Gene silencing is often accompanied by promoter hypermethylation[58]. We calculated the correlation of
250 methylation levels[46] of Paralog A with depletion scores of Paralog B and compared the methylation
251 correlation coefficients to the expression correlation coefficients from PaCT. As shown in Figure 5a,
252 (Supplementary Figure 5a,b; Supplementary Table 2) for some of the pairs, methylation status of Paralog
253 A could be a useful biomarker for dependency on Paralog B. In particular, we could also detect a
254 negative correlation between methylation and gene expression for multiple CpGs in the promoter
255 regions of *FAM50B* and *DNAJC15* (Figure 5b,c, Supplementary Figure 5c). Although correlation does not
256 necessarily imply causation, it is feasible that methylation could underlie low expression of the
257 biomarker paralog in these cases. DNAJC15-DNAJC19 has not been described as a paralog redundancy
258 before, therefore we set out to validate this interaction experimentally. *DNAJC15* expression levels
259 predict sensitivity of cell lines to loss of its paralog *DNAJC19* according to our PaCT analysis (Figure 5d,
260 Supplementary Figure 5d,e). We confirmed the sensitivity to *DNAJC19* knockout in cell lines that do not
261 express *DNAJC15* (Figure 5e) in CRISPR depletion assays (Figure 5f), including cells with high levels of
262 *DNAJC15* as negative controls. Cell lines that do express *DNAJC15* were predicted to be insensitive to
263 loss of *DNAJC19* and accordingly, *DNAJC19*-targeting gRNAs are not depleted from the pool of cells over
264 time. To conclusively demonstrate functional redundancy between the two paralogs, we overexpressed
265 *DNAJC15i* in the sensitive cell line NCI-H1975 and found that we could thereby rescue the dependency
266 on *DNAJC19* (Figure 5g and h).

267

268 **Paralog buffering between chrX- and chrY-encoded genes**

269 Loss of chromosomes have been reported to be frequently occur during cancer development[21].
270 Assessing gene expression and copy number data across The Cancer Genome Atlas (TCGA), did not
271 reveal obvious bimodal distributions for any chromosome except chrY, suggesting that that whole
272 chromosome loss is not frequent enough to be detected in this manner across this dataset
273 (Supplementary Figure 6a,b). As described above, LOY has been associated with increasing age and
274 noted in some cancers derived from male patients[21,26–28]. In agreement with this, a bimodal expression
275 distribution for chrY genes within 1.5% of all male TCGA samples, was observed (Figure 6a). Binning
276 samples by tumour purity shows that LOY is more prevalent in samples with higher tumour purity,
277 indicating that LOY could indeed happen more frequently in cancers compared to adjacent normal tissue

278 (Supplementary Figure 6c). Due to the absence of matched non-tumour samples from TCGA, we used
279 data from the Genotype-Tissue Expression (GTEx) project to estimate the frequency of LOY in normal
280 tissues. In corroboration of our hypothesis, at the same 99th percentile cutoff, no LOY was observed
281 across normal samples GTEx (Supplementary Figure 6d).

282 These studies were further strengthened by analysis of the prevalence of LOY across cancer cell lines
283 used for the AVANA, DRIVE and Sanger screens. LOY was calculated as for the TCGA samples using copy
284 number and expression data and observed in 142 of 459 male cell lines (31% of male, 14% of all cell lines)
285 in our dataset (Figure 6b,c). These studies were supported by analysis of STR profiles for 455 cell lines
286 (46% of cell lines used for PaCT) and analysis of the amelogenin marker for presence or absence of chrY
287 (Figure 6i, Supplementary Table 3)(Figure 6i, Supplementary Table 3). We found that the previous sex
288 assignment was accurate, and LOY status was confirmed for all previously identified cell lines. We
289 further validated the sex chromosome status for a subset of cell lines by a PCR strategy (Figure 6j).

290 We next investigated whether PaCT retrieved any candidate interactions where the biomarker gene is
291 located on chrY to potentially exploit tumour LOY. Only 24 chrY genes were screened in the AVANA,
292 DRIVE or Sanger datasets, 22 of which are part of our paralog families. Interestingly, in four of these
293 pairs, the query genes are located on chrX: *DDX3X-DDX3Y*, *RPS4X-RPS4Y1*, *ZFX-ZFY*, *EIF1AX-EIF1AY*
294 (Figure 6d). These pairs also rank highly in the predictions by DeKegel *et al.*[13]. Notably, all four chrX
295 query genes are genes that escape X chromosome inactivation[59,60], and DDX3X is among a small set of
296 tumour-suppressor genes that escape from X-inactivation (EXITS genes)[61], where mutations occur more
297 frequently in male cancers and co-occur with LOY.

298 In order to validate dependency on the chrX paralog when the chrY paralog is not expressed (or chrY is
299 lost), we used CLIFF (*C*ell *L*ine d*IFF*erences)[62], a web application for the analysis of differences between
300 two sets of cell lines in terms of differential gene or protein expression, DNA copy number, gene signatures,
301 sensitivity to shRNA depletion or CRISPR gene knock-out and other parameters. First, we used k-means
302 clustering to classify cell lines as sensitive and resistant (k=3, leaving out the intermediate group) based on
303 their depletion scores in the AVANA dataset for each of the four chrX paralog hit genes. We then analyzed
304 these groups in CLIFF and looked for the parameters that are most significantly different between the
305 sensitive and resistant cell lines. As a control, we checked that the top gene in the AVANA category is the
306 respective query, i.e. *DDX3X* for the classification run on the *DDX3X* depletion scores (Figure 6e,
307 Supplementary Figure 6e-g). Other AVANA discriminators included some or all of the other chrX hit genes.
308 Conversely, chrY genes, with the respective paralog gene at the top, are the main discriminators based on
309 gene and protein expression, confirming LOY as a potential biomarker that predicts sensitivity to loss of
310 the four selected chrX genes (Figure 6e, Supplementary Figure 6e-g). As expected, LOY cell lines are
311 therefore enriched among the sensitive cell lines for all four chrX genes (Figure 6f, Supplementary Figure
312 6h-j; p-value sensitive vs. resistant = 10^{-4} for all four genes, Fisher's exact test). Accordingly, AVANA
313 depletion scores for *DDX3X* (Figure 6g), *EIF1AX*, *ZFX* and *RPS4X* (Supplementary Figure 6h-m) are generally
314 lower in LOY cell lines than male cell lines. However, some male cell lines are also sensitive to loss of the
315 chrX-encoded paralog, indicating that the genetic buffering by the chrY-encoded gene might be
316 incomplete in some contexts.

317 Consistent with these analyses, a Random Forest (RF) machine-learning model trained with chrY gene and
318 *DDX3X* paralog family gene expression data on the Sanger depletion dataset predicted sensitive and

319 insensitive cells for the AVANA dataset with an accuracy of 0.82. A variable importance analysis revealed
320 *KDM5D*, *DDX3Y*, *EIF1AY* and *RPS4Y1* expression as the top predictors for *DDX3X* sensitivity (Figure 6h).
321 Similar models for *ZFX* and *EIF1AX* were trained on Sanger data, predicted AVANA data with an accuracy of
322 0.715 and 0.82 respectively (Supplementary Figure 6n,o).

323 Genetic rescue experiments were performed to validate the putative functional redundancy between
324 chrX/Y-encoded paralogs. *DDX3X* dependency negatively correlates with the expression levels of *DDX3Y*
325 across a panel of >600 cancer cell lines (Figure 7a) i.e. across the AVANA dataset, low expression of
326 *DDX3Y*- but not other family members correlated with sensitivity to *DDX3X* depletion (Supplementary
327 Figure 7a, b). The *DDX3X-DDX3Y* functional redundancy was previously suggested in a hamster cell line[63]
328 and Raji cells[64] but has not been studied in the context of LOY. In HT-1080 cells, that possess chrY,
329 whereas gRNAs targeting *DDX3X* do not impact the proliferative capacity of these cells, rapid depletion
330 was observed in the context of a gRNA simultaneously targeting *DDX3X* and *DDX3Y* (Figure 7b).
331 Importantly, the effects of the *DDX3X-DDX3Y* dual-specific guide could be completely rescued by
332 expression of gRNA-resistant cDNA constructs for *DDX3X* or *DDX3Y*. Similar results were obtained for
333 another male cancer cell line, HCT 116 (Supplementary Figure 7c). KURAMOCHI cells, derived from a
334 female patient, are dependent on *DDX3X* (Supplementary Figure 7d) demonstrating that buffering of the
335 Y-encoded gene is *a priori* not part of the genetic makeup. Finally, loss of Y-chromosome was confirmed
336 in KNS-42 cells by PCR (Figure 6j). Rapid depletion was observed with gRNAs targeting both *DDX3X* and
337 *DDX3Y* simultaneously as well as gRNA targeting *DDX3X* alone (Figure 7c). Ectopic expression of either
338 *DDX3X* or *DDX3Y* completely reversed the phenotype whereas a functionally unrelated X chromosome
339 located gene X, *ZFX*, did not.

340 These findings were then extended to additional PaCT genes with a putative chrX/Y-encoded
341 redundancy. Sensitivity to *EIF1AX* correlates with the expression of *EIF1AY*, similar to *DDX3X-DDX3Y*,
342 (Figure 7d, Supplementary Figure 7e, f). LOY resulted in a strong dependency on *EIF1AX* (Figure 7f)
343 whereas cells retaining chrY were only sensitive to gRNAs simultaneously targeting *EIF1AX* and *EIF1AY*
344 (Figure 7e). Depletion could be reversed upon expression of gRNA-resistant cDNA constructs encoding
345 for *EIF1AX* or *EIF1AY* (Figure 7e, f). Similar results were obtained with gRNAs targeting *RPS4X* or *RPS4Y*,
346 (Supplementary Figure 7g). In addition to *DDX3X-DDX3Y* and *EIF1AX-EIF1AY*, *ZFX-ZFY* emerged as an
347 additional functionally redundant paralog pair from our PaCT analysis. Sensitivity of cancer cell lines to
348 the loss of *ZFX* correlates with the expression of *ZFY* and, less strongly, with *ZNF711* (Figure 7g,
349 Supplementary Figure 7h,j). As the sensitivity to *ZFX* loss-of-function is less pronounced in KNS-42 cells
350 in the AVANA dataset[42], we turned to female Cal-120 cells for depletion and rescue experiments.
351 CRISPR/Cas9-mediated loss of *ZFX* resulted in depletion of GFP- and gRNA-expressing cells. This
352 phenotype could be rescued with gRNA-resistant cDNA constructs encoding for *ZFX* or *ZFY*, validating
353 the functional redundancy between the two proteins (Figure 7h).

354 In order to confirm that loss of chrY is the causative event in dependency on the paralogs encoded on
355 chrX we designed an approach to engineer removal of chrY (induced LOY, iLOY). Similar to published
356 approaches that have demonstrated loss of the targeted chromosome [65,66], a pool of 18 gRNAs targeting
357 chrY genes was introduced in HT-1080 cells ectopically expressing either *DDX3X* or *ZFX* [62,63] (Figure 7i).
358 LOY was validated by PCR (Figure 6j). Two independent clones were derived and subsequently treated
359 with gRNAs targeting *DDX3X*, *ZFX* and *EIF1AX*. Whereas no phenotype was observed in parental HT-1080
360 cells (Figure 7b,f), LOY clones were sensitive to gRNAs for the chrX-encoded paralog genes. This

361 sensitivity was lost or reduced upon ectopic expression of corresponding gRNA resistant constructs, e.g
362 HT-1080 iLOY *ZFX* are sensitive to a gRNA targeting *DDX3X* whereas HT-1080 iLOY *DDX3X* are not (Figure
363 7j and Supplementary Figure 7j).

364 Altogether, these data suggest that selective targeting of paralogs encoded on the X-chromosome, for
365 which genetic buffering with a chrY-encoded gene exists, might be a generalizable strategy to target LOY
366 tumours. The iLOY experiments validate the loss of chrY as the root cause for this dependency. To the
367 best of our knowledge, these are the first examples for synthetic lethal interactions between paralogs
368 located on the X and Y chromosomes.

369

370 **Discussion**

371 Exploiting distorted genetic buffering in human malignancies represents a promising therapeutic
372 concept. The clinical activity of poly ADP ribose polymerase (PARP) inhibitors in cancers with defects in
373 the homologous recombination-based DNA damage repair pathway[67–69] underlines this point. Paralog
374 genes, originating from gene duplication events, represent an additional subset of these general
375 synthetic lethal genetic interactions where tumour-specific loss of a paralog gene creates a
376 therapeutically exploitable dependency on the remaining paralog gene. In this study, we
377 identified >2000 candidate paralog dependencies relevant to human cancer. We have experimentally
378 validated a subset of these paralog pairs and provide evidence that genetic buffering between the sex
379 chromosomes could provide an attractive therapeutic strategy for human cancers of individuals that
380 have lost the Y chromosome in malignant cells.

381 Our analysis was confined to cancer-relevant interactions that can be identified in the respective cell
382 lines used and genes targeted in publicly available CRISPR/RNAi LOF screens. Due to lack of equal
383 representation of different cancers within the datasets this could lead to a bias for certain tumour types.
384 As described, our discovery pipeline is also "blind" to certain other cases, including uniform expression
385 or depletion of a paralog across all screened cell lines. This is because expression-dependency
386 calculations rely on varying gene expression and depletion scores of one paralog gene across these cell
387 lines. Therefore, approaches like PaCT together with combinatorial genetic screens will further advance
388 our understanding of genetic redundancies. It will be interesting to determine if paralog interactions can
389 be tissue specific and if, within larger families, subsets of genes can have a greater or lesser functional
390 redundancy – a result suggested by our study. If true, this could hint towards the resistance of sub-
391 families and help to functionally annotate understudied paralog genes.

392 As the PaCT approach relies on publicly available screening data, the caveats of the original experiments,
393 such as suboptimal gRNA design in some instances, are carried over into our dataset. The *DNAJC15-*
394 *DNAJC19* example illustrates such a case, where all gRNAs in the public dataset also target a pseudogene
395 sequence. While our experimental validation uses independently designed gRNAs, a potential partial
396 function of the presumed pseudogene will have to be determined. Furthermore, additional
397 investigations will show whether *DNAJC15* and *DNAJC19* indeed both play a role in mitochondrial
398 morphogenesis, and whether *RPP25L* is a *bona fide* subunit of the RNase P/MRP complexes.

399 A number of mechanisms can underlie the paralog loss. In addition to mutation and deletion we provide
400 evidence that epigenetic mechanisms can also play a role. Validated paralog pairs *DNAJC15-DNAJC19*
401 and *FAM50A-FAM50B*, provide examples where high promoter methylation could, in part, account for
402 decreased expression of one paralog gene. This suggests that DNA hypermethylation in tumours could
403 expose novel vulnerabilities that could be exploited therapeutically. Future research will have to clarify if
404 vulnerabilities originating from DNA hypermethylation are stable enough to permit long-term treatment.

405 Our study revealed extensive genetic redundancy between the sex chromosomes. We identified four
406 candidate paralog dependencies (*EIF1AX-EIF1AY*, *DDX3X-DDX3Y*, *RPS4AX-RPS4Y1* and *ZFX-ZFY*) of which
407 we validated three experimentally. Our data suggest that cell lines originating from individuals with chrX
408 and chrY become sensitive to the loss of the chrX-encoded gene upon loss of chrY. While this concept
409 could in principle be exploited therapeutically to treat LOY tumours, premalignant states of mosaic LOY
410 in hematopoiesis or ageing-associated LOY, several hurdles would have to be overcome. It would be
411 important to ensure selectivity of the targeting therapeutic between highly similar paralogs. Although
412 we have not observed LOY across the GTEx dataset, it is possible that alternative mechanisms may also
413 lead to down-regulation of the chrY expressed paralog in normal tissues. While not explicitly addressed,
414 recent studies imply incomplete redundancy for *EIF1AX-EIF1AY* and *DDX3X-DDX3Y* in different contexts
415 in absence of LOY[70–72].

416 Overall, our study identifies cancer-relevant paralog dependencies and provides a framework for
417 validation and future discovery as further panels of functionally validated cancer cell lines become
418 available. While our PaCT approach currently addresses gene expression, deletion and methylation in
419 the paralog genetic space, the approach is generalizable and could be performed analogously for non-
420 paralog genes as queries, and mutations, passenger deletions or other tractable aberrations as
421 biomarkers. We envisage that this will identify additional testable hypotheses for targeted cancer
422 treatment.

423

424 **Materials and Methods**

425 Cell culture

426 All cell lines and the respective media are listed in Supplementary Table 4. Cell lines were regularly
427 checked for mycoplasma, authenticated by STR profiling (Eurofins Genomics) and kept at low passage
428 numbers in humidified incubators at 37°C and 5% CO_2.
429

430 Generation of Cas9- and paralog-expressing cell lines

431 cDNA sequences for Cas9 and paralog genes were human codon-optimized, synthesized and cloned into
432 their respective vector backbone (Supplementary Table 4) at Genscript Biotech Corporation. Cells were
433 lentivirally transduced. Viral particles were generated using the Lenti-X Single Shot System (Clontech).
434 72 hours later, stable transgenic cell pools were selected using puromycin or blasticidin (see
435 Supplementary Table 4 for details).
436

437 CRISPR/Cas9 library design, cloning and virus production

438 The majority of genes in the gRNA library were manually selected from (i) paralog families of 2-5
439 members, (ii) genes frequently deleted in TCGA samples with a focus on deep deletions in lung
440 adenocarcinoma, lung squamous cell carcinoma, colon adenocarcinoma, liver hepatocellular carcinoma,
441 pancreatic adenocarcinoma, ovarian serous cystadenocarcinoma and prostate adenocarcinoma. gRNA
442 sequences were selected to target protein domains (annotated using PFAM domain identifiers) as
443 described[34], as well as control sequences for a total of 9574 gRNAs (Supplementary Table 1).

444 Pooled gRNA oligonucelotides (20-mer target sequences plus cloning adapters;
445 TGCTGTTGACAGTGAGCGCGTCTCTCACCG[20xN]GTTTGGAGACGCCTAGGATCGACGCGGACAACA; Twist
446 Bioscience) were PCR-amplified (0.1 ng DNA input, 24 parallel reactions, 15 cycles). Pooled reactions
447 were purified using the QIAquick PCR purification kit (Qiagen) and digested with BsmBI. The vector
448 backbone (lentiviral vector coexpressing sgRNA, GFP and NeoR, similar to sgETN[73]) was prepared by
449 BsmBI digestion, dephosphorylation and purification as above. Ligation was performed in 14 parallel
450 reactions using T7 ligase and remaining uncut backbone was removed by BsmBI digestion. Ligation
451 products were purified by phenol extraction, transformed into MegaX DH10B T1 electrocompetent
452 bacterial cells (Invitrogen) following manufacturer's protocol and plated on LB/Ampicillin plates.
453 Colonies were combined and maxi-preps were performed at ~7000x colonies per sgRNA.

454 Lentivirus was produced in 293T-Lenti-X cells (Clontech) using 10 µg of library DNA and Ready-to-use
455 Lentiviral Packaging Plasmid Mix (Cellecta, 0.5 µg/µL) per 10 cm dish (20 dishes in total). 293T-Lenti-X
456 were plated without antibiotics and transfected the next day using Lipofectamine LTX & Plus (Thermo
457 Fisher). Medium was changed after 7 h of incubation and viral supernatant was harvested after 48 h.
458 Virus titration was carried out individually for each cell line using three different amounts of viral
459 supernatant in the presence of 8 µg/mL polybrene. Transduction efficacy was evaluated 72 h after
460 infection by measuring GFP expression by flow cytometry.

461 Primer sequences are listed in Supplementary Table 4.
462

463 CRISPR/Cas9 screens

464 Cas9-expressing cell lines were transduced with the sgRNA library at a multiplicity of infection of ~0.3 in
465 the presence of 8 µg/mL polybrene. To this end, 44 x 10^6 cells were cultured in four or more T175 flasks
466 for 12/18 population doublings, representing 1000-fold library coverage. Cell numbers were adapted
467 according to measured GFP percentage after initial infection. From a pellet of the respective cell number
468 at the end point, genomic DNA was isolated using the QIAamp DNA Mini Kit (Qiagen). Amplicons around
469 the sgRNA sequences were PCR amplified (1 µg input per PCR reaction, 29 cycles) with barcoded primers.
470 The total amount of genomic DNA input was calculated by dividing the used total cell number by the
471 assumed value of 6 pg genomic DNA per cell. PCR products were purified using the QIAquick PCR
472 purification kit (Qiagen) and a 2% agarose gel using the QIAquick gel extraction kit (Qiagen). In a second
473 PCR, 10 ng of the purified product per reaction were amplified (5 cycles). The pooled PCR products were
474 purified using the QIAquick PCR purification kit. 50 ng of amplicons were used for the library generation
475 with the TruSeq Nano DNA Library Prep kit for NeoPrep (Illumina). The sequencing was conducted on a
476 HiSeq1500 (Illumina) in rapid mode with the paired end protocol for 50 cycles. For the 7 cell lines (MIA
477 PaCa-2, Hep 3B2.1-7, NCI-H1373, NCI-H1993, NCI-H2009, PC-9, HuP-T4) total read counts ranging from
478 3.1M to 41.6M were generated. Primer sequences are listed in Supplementary Table 4.
479

480 CRISPR/Cas9 library quality control and screen analysis

481 For the plasmid library, 20 million reads were generated and the gRNA representation was tested for
482 uniformity. gRNA counts ranged from 50 to 8708 reads (25th percentile: 983; median: 1682; 75th
483 percentile 2560 reads). For screen analysis, we used the 'mageck test' function of the MAGECK tool
484 (version 0.5.6)[74] to determine the log2-fold-changes and significance estimates (p-values, FDR) for gRNA
485 representation differences between any of the 7 cell lines and those observed in the plasmid library
486 using the following parameters: "mageck test --norm-method control --gene-lfc-method median".

487 To further assess the technical quality of the screens, we overlapped the library with known core-
488 essential (n=625) and never-essential (n=1344) genes constructed from genome scale screens. We found
489 that 307 and 596 gRNAs targeted a subset of the core- and never-essential genes, respectively. We
490 observed a good separation of both guide sets (strictly standardized mean difference < -0.9) and a
491 strong enrichment of core-essential genes in the top depleted genes (AUC > 0.9). Both quality metrics
492 were calculated based on log2-fold-changes from the comparison to the gRNA representation in the
493 plasmid library.

494 To compensate for the variable effect sizes from the different cell lines, we scaled all gene-level log2-
495 fold-changes such that the median log2-fold-change of all never-essential and core-essential genes
496 where set to 0 and –1, respectively. We call this scaled log2-fold-change escore (essentiality score).

497 For hit calling, we selected genes that were specifically depleted (cutoffs for escore < -0.4 and FDR < 0.1)
498 in cell lines that harbor a deletion of a member of the same paralog family (absolute copy number = 0
499 and log2 relative copy number < -1).
500

501 TCGA data

502 For gene expression data, the GDC Data Portal's interface (https://portal.gdc.cancer.gov/) was used to
503 compile all data files that mapped the fields “Program” = “TCGA”, “Data Type” = “Aligned Reads”,
504 “Experimental Strategy” = “RNA-Seq”, and “Workflow Type” = “STAR 2-Pass”. Using the GDC Data
505 Transfer Tool, the data was transferred and pre-processed using samtools[75] collate and fastq to generate
506 FASTQ files, containing the unmapped reads. All samples were subsequently processed with a
507 harmonized RNA-seq pipeline[76].
508 TCGA SNP6 copy number segmentation data was downloaded from NIH GDC
509 (https://portal.gdc.cancer.gov/) on December 3 2018. The segmentation information was obtained from
510 the files *nocnv_grch38.seg.v2.txt. Gene-wise copy numbers were determined by overlapping the
511 segmentation information with Ensembl v86 gene annotation. If a gene was covered by a single segment,
512 the copy number of the segment was assigned to the gene. If a gene was covered by multiple segments,
513 a weighted average copy number was computed based on the size of the overlap between the gene and
514 each segment. Relative copy numbers <= 1.0 were considered as “deep deletion”.
515 The R package TCGAbiolinks (v2.5.9)[77] was used to extract sample and patient information for TCGA
516 samples by using a custom-made R script.
517 The sample cohorts COADREAD, FPPP, GBMLGG, KIPAN, and STES were excluded.
518 Data for TCGA methylation loci plots were downloaded from http://www.bioinfo-zs.com/smartapp/[78].
519 Gene expression levels (log2(TPM)) were plotted against methylation levels of CpGs belonging to islands
520 located in promoter regions of genes of interest.
521

522 Cancer Cell Line Encyclopedia (CCLE) data

523 Cell line names and descriptions (including sex) were taken from the provider’s cell-line data sheet. If a
524 cell line was available from various vendors, the cell-line name was taken from the top rank in a
525 hierarchy of vendors in the following order: ATCC, DSMZ, ECACC, JCRB, ICLC, RIKEN, KCLB.
526 For gene expression, raw FASTQ data for all CCLE cell lines[46] were downloaded via the European
527 Nucleotide Archive (accession number PRJNA523380). All data were processed identically to TCGA data
528 as described above.
529 For copy number determination, SNP6 CEL files were downloaded from https://cghub.ucsc.edu/ in
530 October 2012. Relative copy number segments were computed using the R packages aroma.affymetrix
531 (v3.1.0)[79] and Rawcopy (v1.1)[80]: SNP6 data were processed with the AROMA method CRMA v2, where
532 the 50 samples with the least amount of copy number alterations based on Rawcopy were used to
533 calculate the reference intensities. This was followed by CBS segmentation. Afterwards, the copy
534 number segments were overlapped with Ensembl v86 gene annotation as described for the TCGA data
535 in order to obtain gene-wise relative copy number values. “Deep deletion” status was assigned as for
536 TCGA data. Absolute copy number segments were computed using PICNIC version c_release 2010-10-
537 29[81] with reference files adapted for reference genome hg38 and default parameters. The resulting
538 segments were overlapped with Ensembl v86 gene annotation as for TCGA data in order to obtain gene-
539 wise absolute copy number values.
540 Methylation[46] data are 'CCLE_RRBS_TSS1kb_20181022.txt.gz', downloaded from
541 https://portals.broadinstitute.org/ccle/data. Protein expression[45] data were directly exported from the
542 indicated reference.
543

544 GTEx data

545 GTEx v8 gene expression data (phs000424.v8) where processed as described above (RNA-seq pipeline
546 v2.0 (C-GET)[76]). For 4 samples processing failed, and 582 samples failed QC based on sequence length,
547 GC content, assigned reads, intronic bases, 3'/5' biases, uniquely mapped reads or *GAPDH* detection,
548 and were not included into the final object. Samples from the "Cells - Transformed fibroblast", "Cells -
549 EBV-transformed lymphocytes" and "Cells - Leukemia cell line (CML)" classes are omitted from the data
550 set.
551

552 CRISPR/Cas9 depletion assays

553 All CRISPR/Cas9 depletion assays were conducted as previously described[82]. In brief, gRNA sequences
554 were cloned into their respective vector backbone, typically containing GFP (Supplementary Table 4), at
555 Genscript Biotech Corporation. Lentiviral particles were produced in 293T-Lenti-X (Clontech) cells
556 cultured in DMEM, 10% Tet-system approved FCS, 1X Glutamax, 1X NaPyr. 4 x 10^6 cells were plated in 8
557 ml medium in 10 cm dishes and transiently transfected with 7 µg of plasmid DNA mixed with Lenti-X
558 Packaging Single Shots (VSV-G) (TakaraBio) according to the manufacturer's instructions on the following
559 day. 4 hours after transfection, 6 ml fresh medium was added to the plates. Supernatant was harvested
560 48 hours after transfection, filtered through a 0.45 µm PVDF filter (Millipore) and stored at -80°C in
561 unconcentrated aliquots until further use. Relevant cell lines stably expressing Cas9 (see Supplementary
562 Table 4) were plated at approximately 50 –60 % confluence in 12 or 24 well plates and transduced with
563 250-500 µl of gRNA virus to achieve 10%-95% transduction efficiency. After transduction, the fraction of
564 GFP positive cells was determined at indicated timepoints using flow cytometry.
565 Where cell lines expressing doxycycline-inducible cDNA constructs were included in depletion assays,
566 expression was induced at the start of the experiment by addition of 0.5-1 µg/ml doxycycline to the
567 medium, which was thereafter replenished twice per week.
568

569 siRNA assay
570 Cells were seeded at a density of 4 x 10^5 in 6-well plates in standard culture media. 24 hours after
571 seeding, cells were transfected with OTP Smartpool reagents (Horizon Discovery) targeting *CSTF2*
572 individually or in an equimolar mixture, *CSTF2T* or negative control at a final concentration of 20 nM
573 using RNAiMAX (Invitrogen) as specified by the manufacturer. 24 hours post transfection media was
574 exchanged and cells further incubated for 48 hours. siRNA details are listed in Supplementary Table 4.
575

576 cDNA overexpression

577 Constructs based on the pMSCV-Linker-PGK-Blasti backbone (see Supplementary Table 4) were
578 packaged into viral particles using the Platinum-GP Retrovial Packaging Cell line (). Briefly, 5 x 10^6 cells
579 were plated in 10 cm dishes and co-transfected with 3 µg VSV-G plasmid and 9 µg of the respective
580 construct Lipofectamine LTX (Thermo Fisher) the following day. Medium was exchanged after 16 h and
581 harvested 48 h later for filtration using 0.45 µm PVDF filter (Millipore) and subsequent storage at –80 °C
582 before transduction of target cells and subsequent selection of successfully transduced cells through
583 addition of Blasticidin to the medium.

584 Constructs based on the RT3REN backbone (see Supplementary Table 4) were packaged into lentiviral
585 particles using the Platinum-E packaging cell line (Cell Biolabs). In brief, 600,000 cells were plated in 6

586 well plates and transfected with 2 µg plasmid DNA using 6 µl Lipofectamine LTX reagent (Thermo Fisher).
587 Medium was exchanged after 16 h and harvested 24 h later, filtered through a 0.45 µm PVDF filter
588 (Millipore) and added directly to recipient cells stably expressing an ecotropic receptor (pRRL-RIEH),
589 followed by selection with Geneticin. Lentivirus for pRRL-RIEH was produced in lenti X 293T-Lenti-X
590 (Clontech). 4 x 10^6 cells were plated in 8 ml medium in 10 cm dishes and transiently transfected with 7
591 µg of plasmid DNA mixed with Lenti-X Packaging Single Shots (VSV-G) (TakaraBio) according to the
592 manufacturer's instructions on the following day. 4 hours after transfection, 6 ml fresh medium was
593 added to the plates. Supernatant was harvested 48 hours after transfection, filtered through a 0.45 µm
594 PVDF filter (Millipore) before addition to cells and subsequent selection with Hygromycin.

595

596 Western blot

597 Cells were lysed using RIPA buffer (Sigma) supplemented with HALT protease and phosphatase inhibitor
598 cocktail (Thermo Fisher). Lysates were incubated on ice for 30 min, centrifuged at 14,000 rcf for 20 min
599 at 4°C and protein amounts in the supernatant determined using the Bradford assay (BioRad) according
600 to the manufacturer's instructions. Laemmli buffer was added to samples followed by boiling at 95 °C for
601 5 min. Samples were loaded on a pre-cast gel (Criterion XT Precast 4-12 % Bis-Tris Gel, BioRad), run at
602 150 V for 1.5 hours in XT MOPS running buffer (BioRad) before transfer onto a nitrocellulose membrane
603 (Transblot Turbo Transfer Pack Midi 0.2 µm) for 7 min using the Transblot Turbo Transfer System
604 (BioRad, program: Quickblot Mixed MW, Midi Gel). Membranes were incubated for 1 hour in blocking
605 buffer (10% BSA, 10% PBS-T in water) followed by overnight incubation at 4 °C with primary antibody in
606 BSA antibody buffer (5 % BSA in PBS-T). The next day, membranes were washed three times with PBS-T
607 (10 min per wash) and incubated with secondary antibody in Casein antibody buffer (0,1% Casein in PBS-
608 T) for 1 hour in the dark at room temperature. Membranes were washed three times in PBS-T (10 min
609 per wash) and visualized on an Odyssey CLx imaging system (LI-COR Biosciences).

610 All antibody details can be found in Supplementary Table 4.
611

612 Correlation analysis (PaCT)

613 Depletion data for individual genes were obtained from three studies: DRIVE[44] (2017-10-01), AVANA[42]
614 (21Q1) and Sanger[43] (Release 1). Subsequently, depletion values for every screened gene with unique
615 gene symbols were correlated to expression values (TPM, see above), methylation[46] or protein
616 expression[45] data across the screened cell lines. Methylation data were summarized for genomic regions
617 mapping to a gene. Pearson, Spearman and Kendall correlation coefficients and corresponding p-values
618 were collected. The gene with depletion data is referred to as *query (q)* gene and the gene with
619 expression/methylation data is referred to as *biomarker (b)* for pairwise correlations. Subsequently, data
620 were filtered for genes which are part of a paralog family, such that every pairwise correlation between
621 *q* and *b* is considered if *q* and *b* are part of the same paralog family:

$$A = \{q, b \mid q \wedge b \in of\ same\ paralog\ family\}\ where\ A \subseteq B$$

622 where *B* denotes all correlations between *query* and *biomarker* pairs (screened genes (*q*) and genes with
623 protein and/or mRNA expression values(*b*)) and *A* denotes all correlations for a given paralog family.

624 We used Spearman coefficients and p-values for all subsequent analyses to account for possible non-
625 normal distributions in the data and minimize the impact of outlier values. Due to differences in query
626 and cell line libraries used, and different scoring systems, each sub-dataset that was processed
627 separately (AVANA, Sanger and DRIVE scores for gene and protein expression). For each sub-dataset, we
628 calculated its own cutoff at 3*SD (standard deviation) and additionally filtered for p-value < 0.05. For
629 gene expression data, all p-values at the 3*SD cutoff were highly significant, likely due to the more
630 complete source data for this domain.

631 The complete PaCT results can be found in Supplementary Table 2.
632

633 PaCT exploratory space

634 For all 3,587 paralog families with at least two members, we computed all possible pairwise interactions
635 across members of the same paralog family, including self-interactions. This approach resulted in a total
636 of 3,0841,147 potential pairs. We then assessed the potential of our approach to detect and quantify
637 pairwise dependencies by depletion-expression correlation. Pairs where the query gene was not
638 targeted in any depletion dataset and/or targeted in zero cell lines, and without gene expression data
639 for the biomarker gene expression were labeled as "no info both". Pairs for which information was
640 missing for either depletion or gene expression were labeled as "no info query" and "no info biomarker",
641 respectively. Pairs for which information was available in only a single cell line do not allow calculation
642 of a correlation and were labeled "1 cell line". Pairs for which information was available both for the
643 query and biomarker in at least two cell lines was labeled as "info query & biomarker". Protein
644 expression data were not included in this analysis.
645

646 PaCT simulation analysis

647 To identify the difference between PaCT hit correlations and random correlations, we performed 1000
648 simulations for each gene from each family with significant interactions. For each query gene *q* from
649 each family *f*, we generated a vector of genes *v* with same size as *f*. The new set of genes in *v* contains
650 only the query gene from *f* but the remaining genes in *v* are sampled without replacement from the
651 remaining paralogue families. Then pairwise correlations were computed as above.
652

653 Wilcoxon-test analysis

654 Cell lines were split into sensitive, resistant and intermediate groups using a k-means clustering
655 algorithm with k=3 for the depletion scores of every gene in the DRIVE[44], AVANA[42] and Sanger[43] datasets.
656 For cell lines in the sensitive and resistant bins, gene and protein expression data were collected.
657 Subsequently, a non-parametric test (Wilcoxon test) was conducted for all query-biomarker pairs. p-
658 values were collected and corrected for multiple testing (Benjamini-Hochberg). The query-biomarker
659 pairs were then filtered as described above.
660

661 Random Forest model

662 CCLE gene expression data of chrY-encoded and *DDX3X, EIF1AX, ZFX* and *RPS4X* paralog family genes
663 were used to train a Random Forest (RF) model on the Sanger[43] depletion data. k-means clustering (as

664 described above) was used to separate sensitive and insensitive cell lines. Subsequently, AVANA[42]
665 sensitivity data were predicted using the RF model.
666

667 Ortholog analysis

668 We first converted our list of human paralogs to the best match ortholog in *M. musculus*, *D.*
669 *melanogaster*, *D. rerio*, *C. elegans* or *S. cerevisiae* using DIOPT[83] (v8). Then we added information on
670 each gene's essentiality from OGEE[84] (v2), with a majority vote decision on calling a gene essential or
671 non-essential in cases where more than one dataset with ambiguous calls existed. For all paralog
672 interaction hit pairs, we then checked whether query and biomarker share the same ortholog gene and
673 if so, whether the ortholog is essential.
674

675 Multi-mapping gRNA analysis

676 We downloaded information on dropped gRNAs and gRNA mapping for the AVANA library from
677 https://depmap.org/portal/download/. Based on this information, we extracted the number of dropped,
678 uniquely mapped or multi-mapping gRNAs for each query gene in the list of PaCT pairs.

679

680 LOY inference

681 In addition to gene expression and copy number (CN) data, TCGA, GTEx and CCLE provide annotation of
682 the sex of the patients where a sample/cell line originated from. We calculated (i) the average TPM, (ii)
683 the maximum TPM, (iii) the average raw count, (iv) the average relative CN, and (v) the average absolute
684 CN for all genes located on chrY for all samples. TCGA and GTEx do not provide CN data for chrY. For
685 samples originally annotated as male, we checked whether *all* of their values (i)-(v) for cell lines and (i)-
686 (iii) for tissue samples were below the respective 99th percentile of female samples. If this was the case,
687 we re-annotated the sample as LOY.
688

689 PCR validation of LOY

690 Genotyping primer pairs for different genes on chrX and chrY were designed and tested for specificity.
691 Genomic DNA was extracted from female, male and LOY cells using the QIAamp DNA Mini Kit (Qiagen)
692 following the manufacturer's protocol. PCR was run using AmpliTaqGold DNA polymerase (Thermo
693 Fisher Scientific) with 100 ng genomic DNA as input. 55°C annealing temperature was used for all primer
694 pairs. Resulting amplicons analyzed on a 2% agarose gel. All primer sequences are listed in
695 Supplementary Table 4.
696

697 Induction of LOY

698 One million HT-1080 cells expressing Cas9 (puromycin) and *DDX3X* (blasticidin) or *ZFX* (blasticidin)
699 constructs were transiently transfected with a pool of 18 GFP-containing plasmids encoding for gRNAs
700 targeting different chrY genes (RN-gRNA_429-434, RN-gRNA_441-443, RN-gRNA_458-466 using
701 Lipofectamine 3000 (Thermo Fisher Scientific) according to the manufacturer's instructions. 48 hours

after transfection, GFP-positive cells were isolated by FACS and diluted to obtain single cell clones. Clones were screened for LOY by PCR from genomic DNA (as described above) using standard laboratory techniques. Clones with PCR products for chrX but without PCR products for chrY were selected. gRNA sequences are listed in Supplementary Table 4.

Software and data availability

All calculations were performed in R. Data were visualized using R or GraphPad Prism. All data are publicly available through the indicated references and provided as Supplementary Material, including an R Markdown script containing all code and versioning information to reproduce analyses and figures.

Acknowledgements

We wish to thank Norbert Schweifer, Tamara Tröls, Harald Studensky and Silvia Blaha-Ostermann for technical assistance, Johannes Zuber for help with cloning the paralog gRNA library, and all colleagues at Boehringer Ingelheim RCV Cancer Research Target Discovery for discussions and critical input to the manuscript.

Conflict of Interest

Authors are full time employees of Boehringer Ingelheim.

Author Contributions

A.K., A.H., F.S., T.P., S.O., C.W., M.C., and C.R. conducted wet lab experiments. A.K., A.S., A.P., V.T., F.S., B.M. and R.A.N. conducted bioinformatic analyses. R.A.N. and B.M. conceived study. B.M., R.A.N. and M.P. oversaw study. J.P., S.W., A.S., led paralog library screens. A.S. helped conceptualize study. A.K., B.M. and R.A.N. wrote manuscript with input from all other

727 **Figures and Figure Legends**

728 Figure 1: Proof-of-concept paralog dependency CRISPR screens reveal a functional interaction of *CSTF2*
729 and *CSTF2T*.

730 a-b) Distribution of paralog families in study by family size (a) and gene type (b).
731 c) CRISPR screen results in 7 cancer cell lines. Only genes with escore < -0.4 and FDR < 0.1 are
732 displayed. Shades of green indicate effect size (escore), box color indicates whether paralog
733 family contains deleted gene different from listed gene (del) or not (wt).
734 d) CRISPR/Cas9 depletion assay in cell lines resistant (green) and sensitive (purple) to loss of *CSTF2.*
735 gRNAs targeting positive control genes (*RPA3*, *POLR2A*, *PCNA*), negative controls (*NegCon03/-07*),
736 and *CSTF2* are indicated. Cells were lentivirally transduced with the gRNA plasmid containing GFP;
737 GFP percentage in transduced cell line pool was measured by flow cytometry at the indicated time
738 points and normalized to day 3 post-transduction.
739 e-f) Western blots for *CSTF2* and *CSTF2T* in lysates from indicated cell lines after siRNA treatment
740 (3d). β-actin was used as loading control.
741

742

743 Figure 2: Correlation analysis of public loss-of-function screens yield to identify paralog genetic
744 interactions.

745 a) PaCT analysis workflow and volcano plot of tested pairs by dataset (CYCLOPS, self-interactions;
746 Paralogs, pairwise paralog interactions within same family). See Methods for details.
747 b) Distribution of PaCT correlations (Spearman) by input datasets. Triangles indicate specific hit
748 pairs mentioned in subsequent analyses. Dashed lines mark the 3-standard-deviations cutoff
749 used for hit filtering.
750 c) Distribution of Spearman correlation coefficients of randomly assigned genes to each query
751 compared to the correlation distribution of original PaCT hits.
752 d) Pie chart displaying different categories of query-biomarker pairs across the complete
753 theoretical PaCT exploratory space. Only pairs for which information for both query and
754 biomarker is available can yield hit interactions. See Methods for details.

755 e, f) Expression (e) and depletion score (f) variability distribution of genes involved in hit and non-hit
756 interactions across cell lines.

757 g) Nucleotide sequence similarity difference between hit and non-hit pairs.
758 h) Number of unique hit pairs in paralog families of different size, grouped by type of correlation.
759 i) Percentage of hit pairs identified in each family plotted against family size. Color legend
760 indicates the percentage of genes of the respective family involved in hit interactions, either as
761 query or biomarker.

762 j, k) Percentage of hit interactions per gene as a query (j) and as a biomarker (k) is plotted against
763 percentage of hit interactions per family. Color indicates family size.
764

765

766 Figure 3: Correlation analysis of public loss-of-function screens yield known and novel candidate paralog
767 genetic interactions.

768 a) Overlap of hit pairs between different input datasets. Y-axis shows the number of overlapping
769 pairs by dataset. Comparisons are indicated by dots and lines on the x-axis, colored by type of
770 expression data (gene, protein) and interaction (pos, neg). Inset shows number of hit pairs by
771 dataset.
772 b) Exemplary pairwise correlation matrix for paralog families of 2-4 members and Spearman
773 correlation > 0.42 for at least one pair in the family including CYCLOPS interactions.
774 c) CRISPR/Cas9 depletion assay in cell lines resistant (green) and sensitive (purple) to loss of
775 *FAM50A.* gRNAs targeting positive control genes (*POLR2A*), negative controls (*AAVS1*) and
776 *FAM50A* are indicated. Cells were lentivirally transduced with the gRNA plasmid containing GFP;
777 GFP percentage in the transduced cell line pool was measured by flow cytometry at the
778 indicated time points and normalized to day 3 post-transduction.
779 d) CRISPR/Cas9 depletion assay in cell lines resistant (green) and sensitive (purple) to loss of
780 VPS4*A.* gRNAs targeting positive control genes (*POLR2A*), negative controls (*non-targeting*) and
781 *VPS4A* are indicated. Cells were lentivirally transduced with the gRNA plasmid containing GFP;
782 GFP percentage in the transduced cell line pool was measured by flow cytometry at the
783 indicated time points and normalized to day 3 post-transduction.
784

785

786 Figure 4: Validation of paralog redundancy between *RPP25* and *RPP25L*.

787 a) AVANA-based depletion scores (CERES) for *RPP25L,* color-coded by *RPP25* expression levels.
788 b) Western blot for *RPP25* in indicated cancer cell lines. β-actin was used as loading control.
789 c) CRISPR/Cas9 depletion assay in cell lines predicted to be sensitive (purple) or resistant (green) to
790 loss of *RPP25L*. gRNAs targeting *RPP25L* (gRNA-290, gRNA-291, gRNA-292, gRNA-293), positive
791 controls (*PCNA*, *POLR2A*) and negative controls (non-targeting, *AAVS1*) are indicated. Cells were
792 lentivirally transduced with the gRNA plasmid containing GFP; GFP percentage in transduced cell
793 line pool was measured by flow cytometry at the indicated time points and normalized to day 3
794 post-transduction (n=3 independent replicates of the experiment).
795 d) CRISPR/Cas9 depletion assay as in (c) following ectopic expression of *RPP25* or *RPP25L* in KYSE-
796 150 cells that are sensitive to loss of *RPP25L* (parental). *DNAJC15* expression served as a
797 negative control.
798

799

800 Figure 5: Paralog redundancies for *FAM50A-FAM50B* and *DNAJC15-DNAJC19* can be attributed to
801 expression loss by DNA methylation.

802 a) Scatter plot identifying putative paralog dependencies due to DNA hypermethylation. X-axis:
803 Spearman correlation coefficient between depletion data (CERES score (AVANA data)) and DNA
804 methylation. Y-axis: Spearman correlation coefficient between depletion data (CERES score
805 (AVANA data)) and gene expression (TPM). Pairs with correlation coefficients <|0.2| are
806 displayed as density plots, strongest correlations are labeled.
807 b) Scatter plot of mRNA expression levels (log2(TPM)) of *FAM50B* versus CpG island methylation at
808 indicated loci across tumour types from TCGA. Samples from bladder urothelial carcinoma
809 (BLCA), prostate adenocarcinoma (PRAD) and stomach adenocarcinoma (STAD) studies are
810 highlighted.
811 c) Scatter plot of mRNA expression levels (log2(TPM)) of *DNAJC15* versus CpG island methylation at
812 indicated loci across tumour types from TCGA. Samples from bladder urothelial carcinoma
813 (BLCA), prostate adenocarcinoma (PRAD) and stomach adenocarcinoma (STAD) studies are
814 highlighted.
815 d) Boxplot summarizing expression data (log2(TPM)) for members of the *DNAJC19-DNAJC15*
816 paralog family in cell lines resistant and sensitive to *DNAJC19* loss.
817 e) Western blot of *DNAJC15* levels in selected sensitive (CAL-12T, NCI-H1915, NCI-H1975) and
818 resistant (DMS53, IPC-298, SCC-25) cell lines. β-actin was included as a loading control.
819 f) CRISPR/Cas9 depletion assay in cell lines predicted to be sensitive (purple) or resistant (green) to
820 loss of *DNAJC19*. gRNAs targeting *DNAJC19* (gRNA-318, gRNA-523, gRNA-565, gRNA-566),
821 positive controls (*PCNA*, *POLR2A*) and negative controls (non-targeting, *AAVS1*) are indicated.
822 Cells were lentivirally transduced with the gRNA plasmids also containing a GFP expression
823 cassette. The percentage of GFP expressing cells in the transduced cell line pool was measured
824 by flow cytometry at the indicated time points and normalized to day 3 post-transduction (n=3
825 independent replicates of the experiment).
826 g) CRISPR/Cas9 depletion assay in cell lines following ectopic expression of *DNAJC15* in NCI-H1975
827 cells that are sensitive to loss of *DNAJC19*. Expression was induced by addition of 1 µg/ml
828 doxycycline to the medium at the start of the experiment, which was replenished twice per
829 week. Cells were lentivirally transduced with a gRNA targeting *DNAJC19* (gRNA-318), positive
830 control (*POLR2A*) or negative control (non-targeting). The plasmid also expresses GFP. The
831 percentage of GFP-positive cells in transduced cell line pool was measured by flow cytometry at
832 the indicated time points and normalized to day 3 post-transduction (n=2 independent
833 replicates of the experiment).
834 h) Western blot for RPP25, DNAJC15, and DNAJC19 in NCI-H1975 cells expressing the indicated
835 overexpression constructs upon culture in the presence of doxycycline (1 µg/ml) for 72 hours. β-
836 actin was included as a loading control.
837

838

839 Figure 6: Loss of chrY as potential biomarker for paralog dependencies between sex chromosome genes.

840 a) Distribution of average gene expression (TPM) across genes located on chrY for TCGA samples
841 for which data were available. Sex (male, female) as annotated in TCGA or inferred (LOY) as
842 described in Methods.
843 b) As in (a) for cell lines (CCLE) with available gene expression data.
844 c) As in (b) for average relative copy number (CN).
845 d) Schematic depiction of chrX and chrY with location of interacting paralogs indicated.
846 e) Analysis of factors that are most significantly different between *DDX3X*-loss-sensitive and
847 *DDX3X*-loss-resistant cell lines, as defined using k-means clustering based on AVANA data. For
848 each data domain, the most significant discriminators are displayed.
849 f) Sensitive vs. resistant cell lines (as in (e)) by sex (as in (b and c)).
850 g) *DDX3X* sensitivity (CERES depletion score from AVANA dataset) by sex (as in (b and c)). p-values
851 were calculated using a two-sided Fisher's exact test for count data with Monte-Carlo-simulated
852 p-value (based on 10000 replicates).
853 h) Variable importance plot for Random Forest model to predict *DDX3X* sensitivity. Gene
854 expression values were used as variables for the Indicated genes on y-axis.
855 i) Fraction of cell lines that harbor chrX and chrY or chrX only, grouped by sex ((as in (b and c)), as
856 assessed by the amelogenin marker in standard STR analysis.
857 j) PCR validation of sex chromosome status in selected cell lines used for further analyses. 8 chrY-
858 specific primer pairs and 2 chrX-specific primer pairs were tested in female patient-derived
859 (KURAMOCHI and Cal-120), male patient-derived chrY retaining (HT-1080 and HCT 116), and
860 male LOY cells (KNS-42).
861

862

863 Figure 7: Validation of chrX-chrY paralog dependencies.

864 a) AVANA-based depletion scores (CERES) for *DDX3X,* color-coded by *DDX3Y* expression levels.
865 b) CRISPR/Cas9 depletion assay in male HT-1080 cells that carry chrY. gRNAs targeting a positive
866 control gene (*PCNA*), negative control locus (*AAVS1*), *DDX3X* (gRNA-395, gRNA-396) and *DDX3X*
867 and *DDX3Y* simultaneously are indicated. Cells were lentivirally transduced with the gRNA
868 plasmid containing GFP; GFP percentage in transduced cell line pool was measured by flow
869 cytometry at the indicated time points and normalized to day 3 post-transduction. Cells were
870 additionally transduced with empty vector (control), unrelated cDNA encoding *ZFX* (control), or
871 rescue constructs with cDNA encoding *DDX3X* or *DDX3Y*. Points in line graph represent mean,
872 and error bars denote the standard deviation (n= 3 independent experiments).
873 c) CRISPR/Cas9 depletion assay in male KNS-42 cells that lost chrY (LOY). Assay, gRNAs and cDNA
874 constructs as in (b). Points in line graph represent mean, and error bars denote the standard
875 deviation (n= 3 independent experiments).
876 d) AVANA-based depletion scores (CERES) for *EIF1AX,* color-coded by *EIF1AY* expression levels.
877 e) CRISPR/Cas9 depletion assay in male HCT 116 cells that carry chrY. gRNAs targeting positive
878 control (*PCNA*), negative control (*AAVS1*), and *EIF1AX* and *EIF1AY* simultaneously are indicated.
879 Cells were additionally transduced with empty vector (control), unrelated cDNA encoding *ZFX*
880 (control), or rescue constructs with cDNA encoding *EIF1AX* or *EIF1AY*. Assay as in (b), points in
881 line graph represent mean, and error bars denote the standard deviation (n= 3 independent
882 experiments).
883 f) CRISPR/Cas9 depletion assay in male KNS-42 cells that lost chrY (LOY). gRNAs targeting positive
884 control (*PCNA*), negative control (*AAVS1*), *EIF1AX, EIF1AX/EIF1AXP1,* and *EIF1AX/EIF1AXP1* and
885 *EIF1AY* simultaneously are indicated. Cells were additionally transduced with empty vector
886 (control) or rescue constructs with cDNA encoding *EIF1AX* or *EIF1AY*. *EIF1AX/XP1* indicates
887 *EIF1AX* and the *EIF1AXP1* pseudogene. Assay as in (b), points in line graph represent mean, and
888 error bars denote the standard deviation (n= 3 independent experiments).
889 g) AVANA-based depletion scores (CERES) for *ZFX,* color-coded by *ZFY* expression levels.
890 h) CRISPR/Cas9 depletion assay in female Cal-120 cells. gRNAs targeting positive control (*PCNA*),
891 negative control (*AAVS1*), and *ZFX* (gRNA-569, gRNA-571) are indicated. Cells were additionally
892 transduced with empty vector (control) or rescue constructs with cDNA encoding *ZFX* or *ZFY*.
893 Assay as in (b), points in line graph represent mean, and error bars denote the standard
894 deviation (n= 3 independent experiments).
895 i) Schematic depiction of workflow for induction of LOY in male HT-1080 cells expressing Cas9 and
896 DDX3X or ZFX.
897 j) CRISPR/Cas9 depletion assay in male HT-1080 cells where LOY was induced. Two clones each
898 expressing cDNA constructs encoding DDX3X or ZFX were transduced with gRNAs targeting
899 positive control (*POLR2A*), negative control (*AAVS1*), *DDX3X,* ZFX or *EIF1AX/EIF1AXP1.*
900 *EIF1AX/XP1* indicates *EIF1AX* and the *EIF1AXP1* pseudogene. Assay as in (b), points in line graph
901 represent mean, and error bars denote the standard deviation (n= 3 independent experiments).

902

903

904 **References**

905

906

907 1. Ihmels, J., Collins, S. R., Schuldiner, M., Krogan, N. J. & Weissman, J. S. Backup without redundancy:
908 genetic interactions reveal the cost of duplicate gene loss. *Mol Syst Biol* **3**, 86 (2007).

909 2. Vavouri, T., Semple, J. I. & Lehner, B. Widespread conservation of genetic redundancy during a billion
910 years of eukaryotic evolution. *Trends Genet* **24**, 485–488 (2008).

911 3. Dandage, R. & Landry, C. R. Paralog dependency indirectly affects the robustness of human cells. *Mol*
912 *Syst Biol* **15**, e8871 (2019).

913 4. Ohno, S. Evolution by Gene Duplication. (1970) doi:10.1007/978-3-642-86659-3.

914 5. Aldana, M., Balleza, E., Kauffman, S. & Resendiz, O. Robustness and evolvability in genetic regulatory
915 networks. *J Theor Biol* **245**, 433–448 (2007).

916 6. Muller, F. L. *et al.* Passenger deletions generate therapeutic vulnerabilities in cancer. *Nature* **488**,
917 337–342 (2012).

918 7. Ehrenhöfer-Wölfer, K. *et al.* SMARCA2-deficiency confers sensitivity to targeted inhibition of
919 SMARCA4 in esophageal squamous cell carcinoma cell lines. *Sci Rep-uk* **9**, 11661 (2019).

920 8. Hoffman, G. R. *et al.* Functional epigenetics approach identifies BRM/SMARCA2 as a critical synthetic
921 lethal target in BRG1-deficient cancers. *Proc National Acad Sci* **111**, 3128–3133 (2014).

922 9. Oike, T. *et al.* A Synthetic Lethality–Based Strategy to Treat Cancers Harboring a Genetic Deficiency in
923 the Chromatin Remodeling Factor BRG1. *Cancer Res* **73**, 5508–5518 (2013).

924 10. Helming, K. C. *et al.* ARID1B is a specific vulnerability in ARID1A-mutant cancers. *Nat Med* **20**, 251–
925 254 (2014).

926 11. Lelij, P. van der *et al.* Synthetic lethality between the cohesin subunits STAG1 and STAG2 in diverse
927 cancer contexts. *Elife* **6**, e26980 (2017).

928 12. Benedetti, L., Cereda, M., Monteverde, L., Desai, N. & Ciccarelli, F. D. Synthetic lethal interaction
929 between the tumour suppressor STAG2 and its paralog STAG1. *Oncotarget* **5**, 37619–37632 (2014).

930 13. Kegel, B. D., Quinn, N., Thompson, N. A., Adams, D. J. & Ryan, C. J. Comprehensive prediction of
931 synthetic lethality between paralog pairs in cancer cell lines. *BioRxiv* (2020)
932 doi:10.1101/2020.12.16.423022.

933 14. Tsherniak, A. *et al.* Defining a Cancer Dependency Map. *Cell* **170**, 564-576.e16 (2017).

934 15. Parrish, P. C. R. *et al.* Discovery of synthetic lethal and tumor suppressive paralog pairs in the human
935 genome. *Biorxiv* 2020.12.20.423710 (2020) doi:10.1101/2020.12.20.423710.

936 16. Gonatopoulos-Pournatzis, T. *et al.* Genetic interaction mapping and exon-resolution functional
937 genomics with a hybrid Cas9-Cas12a platform. *Nat Biotechnol* **38**, 638–648 (2020).

938 17. Dede, M., McLaughlin, M., Kim, E. & Hart, T. Multiplex enCas12a screens detect functional buffering
939 among paralogs otherwise masked in monogenic Cas9 knockout screens. *Genome Biol* **21**, 262 (2020).

940 18. Kegel, B. D. & Ryan, C. J. Paralog buffering contributes to the variable essentiality of genes in cancer
941 cell lines. *Plos Genet* **15**, e1008466 (2019).

942 19. Thompson, N. A. *et al.* Combinatorial CRISPR screen identifies fitness effects of gene paralogues. *Nat*
943 *Commun* **12**, 1302 (2021).

944 20. Viswanathan, S. R. *et al.* Genome-scale analysis identifies paralog lethality as a vulnerability of
945 chromosome 1p loss in cancer. *Nat Genet* **50**, 937–943 (2018).

946 21. Duijf, P. H. G., Schultz, N. & Benezra, R. Cancer cells preferentially lose small chromosomes. *Int J*
947 *Cancer* **132**, 2316–2326 (2013).

948 22. Li, C. H. *et al.* Sex differences in oncogenic mutational processes. *Nat Commun* **11**, 4330 (2020).

949 23. Wright, D. J. *et al.* Genetic variants associated with mosaic Y chromosome loss highlight cell cycle
950 genes and overlap with cancer susceptibility. *Nat Genet* **49**, 674–679 (2017).

951 24. Kaneko, S. & Li, X. X chromosome protects against bladder cancer in females via a KDM6A-
952 dependent epigenetic mechanism. *Sci Adv* **4**, eaar5598 (2018).

953 25. Spatz, A., Borg, C. & Feunteun, J. X-Chromosome Genetics and Human Cancer. *Nat Rev Cancer* **4**,
954 617–629 (2004).

955 26. Hunter, S., Gramlich, T., Abbott, K. & Varma, V. Y chromosome loss in esophageal carcinoma: An in
956 situ hybridization study. *Genes Chromosomes Cancer* **8**, 172–177 (1993).

957 27. Agahozo, M. C. *et al.* Loss of Y-Chromosome during Male Breast Carcinogenesis. *Cancers* **12**, 631
958 (2020).

959 28. Minner, S. *et al.* Y chromosome loss is a frequent early event in urothelial bladder cancer. *Pathology*
960 **42**, 356–359 (2010).

961 29. Lin, S.-H. *et al.* Mosaic chromosome Y loss is associated with alterations in blood cell counts in UK
962 Biobank men. *Sci Rep-uk* **10**, 3655 (2020).

963 30. Forsberg, L. A. *et al.* Mosaic loss of chromosome Y in peripheral blood is associated with shorter
964 survival and higher risk of cancer. *Nat Genet* **46**, 624–628 (2014).

965 31. Thompson, D. J. *et al.* Genetic predisposition to mosaic Y chromosome loss in blood. *Nature* **575**,
966 652–657 (2019).

967 32. Guo, X. *et al.* Mosaic loss of human Y chromosome: what, how and why. *Hum Genet* **139**, 421–446
968 (2020).

969 33. Lau, Y.-F. C. Y chromosome in health and diseases. *Cell Biosci* **10**, 97 (2020).

970 34. Shi, J. *et al.* Discovery of cancer drug targets by CRISPR-Cas9 screening of protein domains. *Nat*
971 *Biotechnol* **33**, 661–7 (2015).

972 35. Dass, B. *et al.* Loss of polyadenylation protein τCstF-64 causes spermatogenic defects and male
973 infertility. *Proc National Acad Sci* **104**, 20374–20379 (2007).

974 36. Romeo, V., Griesbach, E. & Schümperli, D. CstF64: Cell Cycle Regulation and Functional Role in 3′
975 End Processing of Replication-Dependent Histone mRNAs. *Mol Cell Biol* **34**, 4272–4284 (2014).

976 37. Yao, C. *et al.* Overlapping and distinct functions of CstF64 and CstF64τ in mammalian mRNA 3′
977 processing. *Rna* **19**, 1781–1790 (2013).

978 38. Youngblood, B. A., Grozdanov, P. N. & MacDonald, C. C. CstF-64 supports pluripotency and regulates
979 cell cycle progression in embryonic stem cells through histone 3′ end processing. *Nucleic Acids Res* **42**,
980 8330–8342 (2014).

981 39. Minvielle-Sebastia, L., Winsor, B., Bonneaud, N. & Lacroute, F. Mutations in the yeast RNA14 and
982 RNA15 genes result in an abnormal mRNA decay rate; sequence analysis reveals an RNA-binding domain
983 in the RNA15 protein. *Mol Cell Biol* **11**, 3075–3087 (1991).

984 40. Youngblood, B. A. & MacDonald, C. C. CstF-64 is necessary for endoderm differentiation resulting in
985 cardiomyocyte defects. *Stem Cell Res* **13**, 413–421 (2014).

986 41. Mohr, S. E., Smith, J. A., Shamu, C. E., Neumüller, R. A. & Perrimon, N. RNAi screening comes of age:
987 improved techniques and complementary approaches. *Nat Rev Mol Cell Bio* **15**, 591–600 (2014).

988 42. Meyers, R. M. *et al.* Computational correction of copy number effect improves specificity of CRISPR–
989 Cas9 essentiality screens in cancer cells. *Nat Genet* **49**, 1779–1784 (2017).

990 43. Behan, F. M. *et al.* Prioritization of cancer therapeutic targets using CRISPR–Cas9 screens. *Nature*
991 **568**, 511–516 (2019).

992 44. McDonald, E. R. *et al.* Project DRIVE: A Compendium of Cancer Dependencies and Synthetic Lethal
993 Relationships Uncovered by Large-Scale, Deep RNAi Screening. *Cell* **170**, 577-592.e10 (2017).

994 45. Nusinow, D. P. *et al.* Quantitative Proteomics of the Cancer Cell Line Encyclopedia. *Cell* **180**, 387-
995 402.e16 (2020).

996 46. Ghandi, M. *et al.* Next-generation characterization of the Cancer Cell Line Encyclopedia. *Nature* **569**,
997 503–508 (2019).

998 47. Fortin, J.-P. *et al.* Multiple-gene targeting and mismatch tolerance can confound analysis of genome-
999 wide pooled CRISPR screens. *Genome Biol* **20**, 21 (2019).

1000 48. Nijhawan, D. *et al.* Cancer Vulnerabilities Unveiled by Genomic Loss. *Cell* **150**, 842–854 (2012).

1001 49. Paolella, B. R. *et al.* Copy-number and gene dependency analysis reveals partial copy loss of wild-
1002 type SF3B1 as a novel cancer vulnerability. *Elife* **6**, e23268 (2017).

1003 50. Oughtred, R. *et al.* The BioGRID database: A comprehensive biomedical resource of curated protein,
1004 genetic, and chemical interactions. *Protein Sci* **30**, 187–200 (2021).

1005 51. Modos, D. *et al.* Identification of critical paralog groups with indispensable roles in the regulation of
1006 signaling flow. *Sci Rep-uk* **6**, 38588 (2016).

1007 52. Neggers, J. E. *et al.* Synthetic Lethal Interaction between the ESCRT Paralog Enzymes VPS4A and
1008 VPS4B in Cancers Harboring Loss of Chromosome 18q or 16q. *Cell Reports* **33**, 108493 (2020).

1009 53. Szymańska, E. *et al.* Synthetic lethality between VPS4A and VPS4B triggers an inflammatory response
1010 in colorectal cancer. *Embo Mol Med* **12**, e10812 (2020).

1011 54. Wu, J. *et al.* Cryo-EM Structure of the Human Ribonuclease P Holoenzyme. *Cell* **175**, 1393-1404.e11
1012 (2018).

1013 55. Welting, T. J. M., Kikkert, B. J., Venrooij, W. J. van & Pruijn, G. J. M. Differential association of protein
1014 subunits with the human RNase MRP and RNase P complexes. *Rna* **12**, 1373–1382 (2006).

1015 56. GUERRIER-TAKADA, C., EDER, P. S., GOPALAN, V. & ALTMAN, S. Purification and characterization of
1016 Rpp25, an RNA-binding protein subunit of human ribonuclease P. *Rna* **8**, 290–295 (2002).

1017 57. Goldfarb, K. C. & Cech, T. R. Targeted CRISPR disruption reveals a role for RNase MRP RNA in human
1018 preribosomal RNA processing. *Gene Dev* **31**, 59–71 (2017).

1019 58. Jones, P. A. Functions of DNA methylation: islands, start sites, gene bodies and beyond. *Nat Rev*
1020 *Genet* **13**, 484–492 (2012).

1021 59. Tukiainen, T. *et al.* Landscape of X chromosome inactivation across human tissues. *Nature* **550**, 244–
1022 248 (2017).

1023 60. Balaton, B. P., Cotton, A. M. & Brown, C. J. Derivation of consensus inactivation status for X-linked
1024 genes from genome-wide studies. *Biol Sex Differ* **6**, 35 (2015).

1025 61. Dunford, A. *et al.* Tumor-suppressor genes that escape from X-inactivation contribute to cancer sex
1026 bias. *Nat Genet* **49**, 10–16 (2016).

1027 62. Wernitznig, A. *et al.* Abstract 3227: CLIFF, a bioinformatics software tool to explore molecular
1028 differences between two sets of cancer cell lines. 3227–3227 (2020) doi:10.1158/1538-7445.am2020-
1029 3227.

1030 63. Sekiguchi, T., Iida, H., Fukumura, J. & Nishimoto, T. Human DDX3Y, the Y-encoded isoform of RNA
1031 helicase DDX3, rescues a hamster temperature-sensitive ET24 mutant cell line with a DDX3X mutation.
1032 *Exp Cell Res* **300**, 213–222 (2004).

1033 64. Wang, T. *et al.* Identification and characterization of essential genes in the human genome. *Science*
1034 **350**, 1096–1101 (2015).

1035 65. Zuo, E. *et al.* CRISPR/Cas9-mediated targeted chromosome elimination. *Genome Biol* **18**, 224 (2017).

1036 66. Adikusuma, F., Williams, N., Grutzner, F., Hughes, J. & Thomas, P. Targeted Deletion of an Entire
1037 Chromosome Using CRISPR/Cas9. *Mol Ther* **25**, 1736–1738 (2017).

1038 67. Fong, P. C. *et al.* Inhibition of Poly(ADP-Ribose) Polymerase in Tumors from BRCA Mutation Carriers.
1039 *New Engl J Medicine* **361**, 123–134 (2009).

1040 68. Bryant, H. E. *et al.* Specific killing of BRCA2-deficient tumours with inhibitors of poly(ADP-ribose)
1041 polymerase. *Nature* **434**, 913–917 (2005).

1042 69. Farmer, H. *et al.* Targeting the DNA repair defect in BRCA mutant cells as a therapeutic strategy.
1043 *Nature* **434**, 917–921 (2005).

1044 70. Godfrey, A. K. *et al.* Quantitative analysis of Y-Chromosome gene expression across 36 human
1045 tissues. *Genome Res* **30**, 860–873 (2020).

1046 71. Venkataramanan, S., Calviello, L., Wilkins, K. & Floor, S. N. DDX3X and DDX3Y are redundant in
1047 protein synthesis. *Biorxiv* 2020.09.30.319376 (2020) doi:10.1101/2020.09.30.319376.

1048 72. Szappanos, D. *et al.* The RNA helicase DDX3X is an essential mediator of innate antimicrobial
1049 immunity. *Plos Pathog* **14**, e1007397 (2018).

1050 73. Michlits, G. *et al.* Multilayered VBC score predicts sgRNAs that efficiently generate loss-of-function
1051 alleles. *Nat Methods* 1–9 (2020) doi:10.1038/s41592-020-0850-8.

1052 74. Li, W. *et al.* MAGeCK enables robust identification of essential genes from genome-scale
1053 CRISPR/Cas9 knockout screens. *Genome Biol* **15**, 554 (2014).

1054 75. Li, H. *et al.* The Sequence Alignment/Map format and SAMtools. *Bioinformatics* **25**, 2078–2079
1055 (2009).

1056 76. Hofmann, M. H. *et al.* BI-3406, a potent and selective SOS1::KRAS interaction inhibitor, is effective in
1057 KRAS-driven cancers through combined MEK inhibition. *Cancer Discov* CD-20-0142 (2020)
1058 doi:10.1158/2159-8290.cd-20-0142.

1059 77. Colaprico, A. *et al.* TCGAbiolinks: an R/Bioconductor package for integrative analysis of TCGA data.
1060 *Nucleic Acids Res* **44**, e71–e71 (2016).

1061 78. Li, Y., Ge, D. & Lu, C. The SMART App: an interactive web application for comprehensive DNA
1062 methylation analysis and visualization. *Epigenet Chromatin* **12**, 71 (2019).

1063 79. Bengtsson, H., Simpson, K., Bullard, J. & Hansen, K. aroma.affymetrix: A generic framework in R for
1064 analyzing small to very large Affymetrix data sets in bounded memory. *Report 745, Department of*
1065 *Statistics, University of California, Berkeley, 2008* (2008).

1066 80. Mayrhofer, M., Viklund, B. & Isaksson, A. Rawcopy: Improved copy number analysis with Affymetrix
1067 arrays. *Sci Rep-uk* **6**, 36158 (2016).

1068 81. Greenman, C. D. *et al.* PICNIC: an algorithm to predict absolute allelic copy number variation with
1069 microarray cancer data. *Biostatistics* **11**, 164–175 (2010).

1070 82. Hörmann, A. *et al.* RIOK1 kinase activity is required for cell survival irrespective of MTAP status.
1071 *Oncotarget* **9**, 28625–28637 (2018).

1072 83. Hu, Y. *et al.* An integrative approach to ortholog prediction for disease-focused and other functional
1073 studies. *Bmc Bioinformatics* **12**, 357 (2011).

1074 84. Chen, W.-H., Lu, G., Chen, X., Zhao, X.-M. & Bork, P. OGEE v2: an update of the online gene
1075 essentiality database with special focus on differentially essential genes in human cancer cell lines.
1076 *Nucleic Acids Res* **45**, D940–D944 (2016).

1077

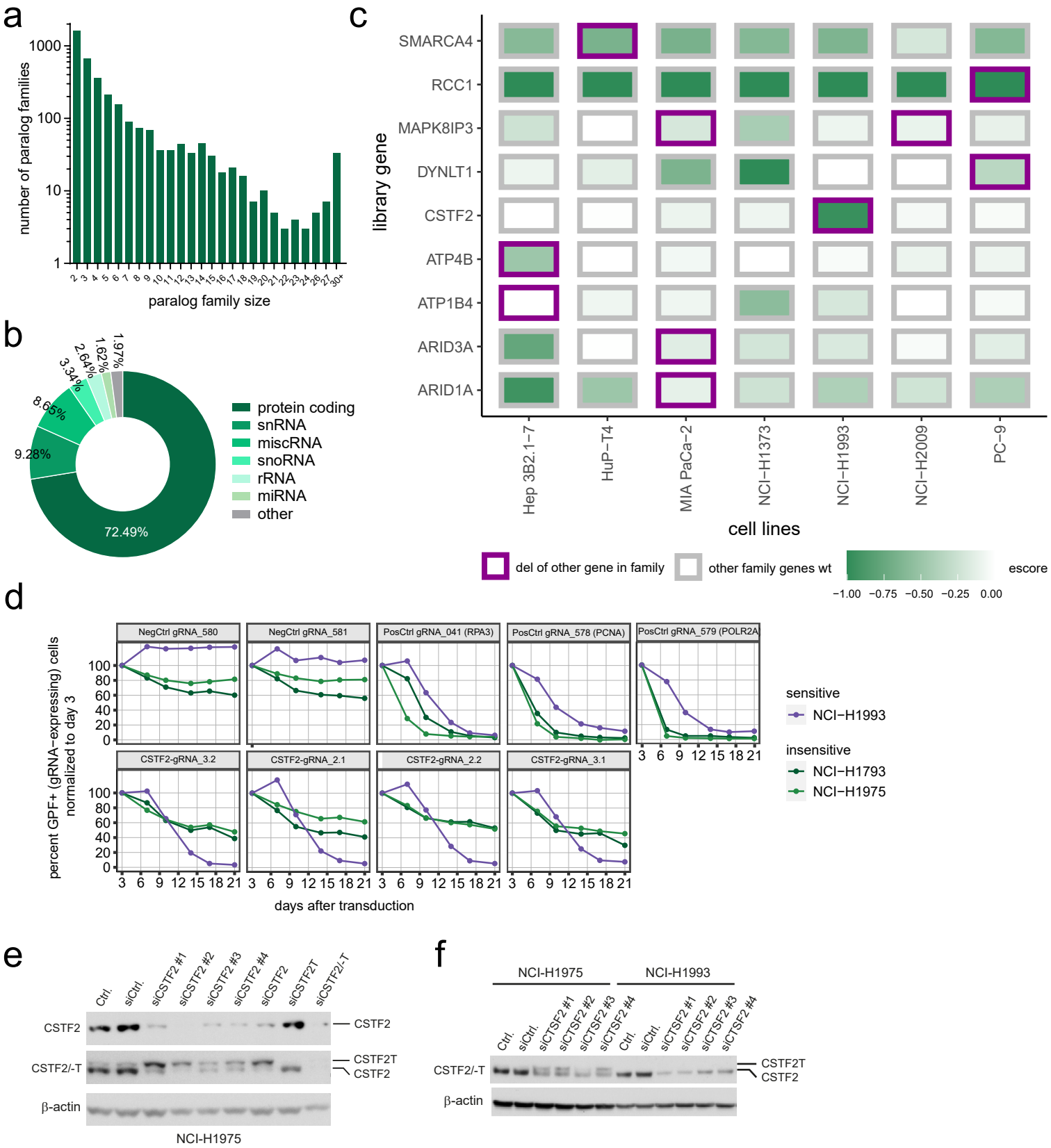
a
number of paralog families
paralog family size
b
protein coding
snRNA
miscRNA
snoRNA
rRNA
miRNA
other
72.49%
9.28%
8.65%
3.34%
2.64%
1.62%
1.97%
c
library gene
SMARCA4
RCC1
MAPK8IP3
DYNLT1
CSTF2
ATP4B
ATP1B4
ARID3A
ARID1A
Hep 3B2.1−7
HuP−T4
MIA PaCa−2
NCI−H1373
NCI−H1993
NCI−H2009
PC−9
cell lines
del of other gene in family
other family genes wt
escore
−1.00 −0.75 −0.50 −0.25 0.00
d
NegCtrl gRNA_580
NegCtrl gRNA_581
PosCtrl gRNA_041 (RPA3)
PosCtrl gRNA_578 (PCNA)
PosCtrl gRNA_579 (POLR2A)
CSTF2-gRNA_3.2
CSTF2-gRNA_2.1
CSTF2-gRNA_2.2
CSTF2-gRNA_3.1
percent GPF+ (gRNA−expressing) cells normalized to day 3
days after transduction
sensitive
NCI−H1993
insensitive
NCI−H1793
NCI−H1975
e
Ctrl.
siCtrl.
siCSTF2 #1
siCSTF2 #2
siCSTF2 #3
siCSTF2 #4
siCSTF2
siCSTF2T
siCSTF2/-T
CSTF2
CSTF2/-T
β-actin
CSTF2T
NCI-H1975
f
NCI-H1975
NCI-H1993

Figure 1

Figure 2

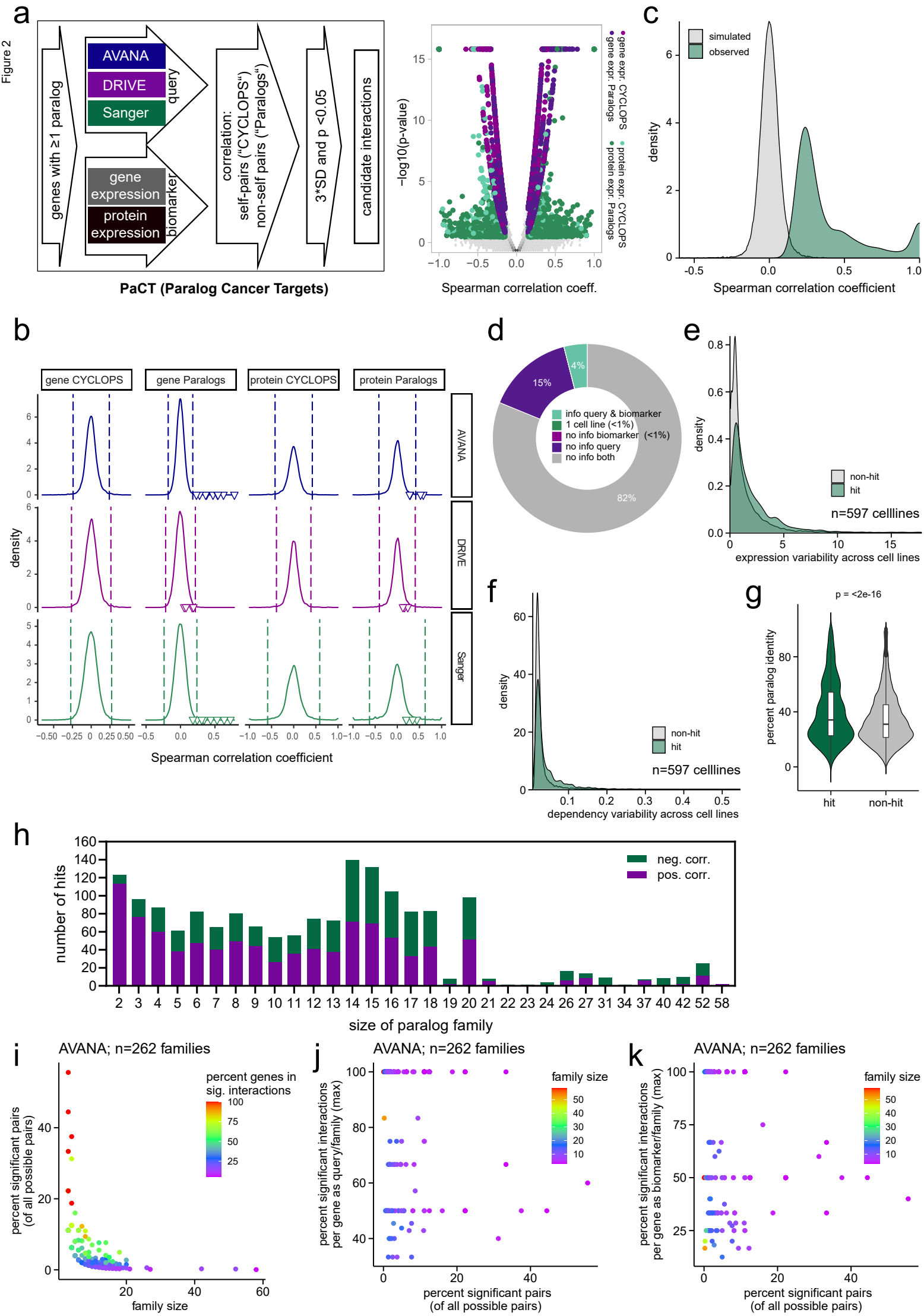
a
genes with ≥1 paralog
AVANA
DRIVE
Sanger
query
gene expression
protein expression
biomarker
correlation:
self-pairs ("CYCLOPS")
non-self pairs ("Paralogs")
3*SD and p <0.05
candidate interactions
PaCT (Paralog Cancer Targets)
−log10(p-value)
Spearman correlation coeff.
gene expr. CYCLOPS
gene expr. Paralogs
protein expr. CYCLOPS
protein expr. Paralogs
c
simulated
observed
density
Spearman correlation coefficient
b
gene CYCLOPS
gene Paralogs
protein CYCLOPS
protein Paralogs
AVANA
DRIVE
Sanger
density
Spearman correlation coefficient
d
4%
15%
82%
info query & biomarker
1 cell line (<1%)
no info biomarker (<1%)
no info query
no info both
e
density
non-hit
hit
n=597 celllines
expression variability across cell lines
f
density
non-hit
hit
n=597 celllines
dependency variability across cell lines
g
p = <2e-16
percent paralog identity
hit
non-hit
h
number of hits
neg. corr.
pos. corr.
size of paralog family
i
AVANA; n=262 families
percent genes in sig. interactions
percent significant pairs (of all possible pairs)
family size
j
AVANA; n=262 families
family size
percent significant interactions per gene as query/family (max)
percent significant pairs (of all possible pairs)
k
AVANA; n=262 families
family size
percent significant interactions per gene as biomarker/family (max)
percent significant pairs (of all possible pairs)

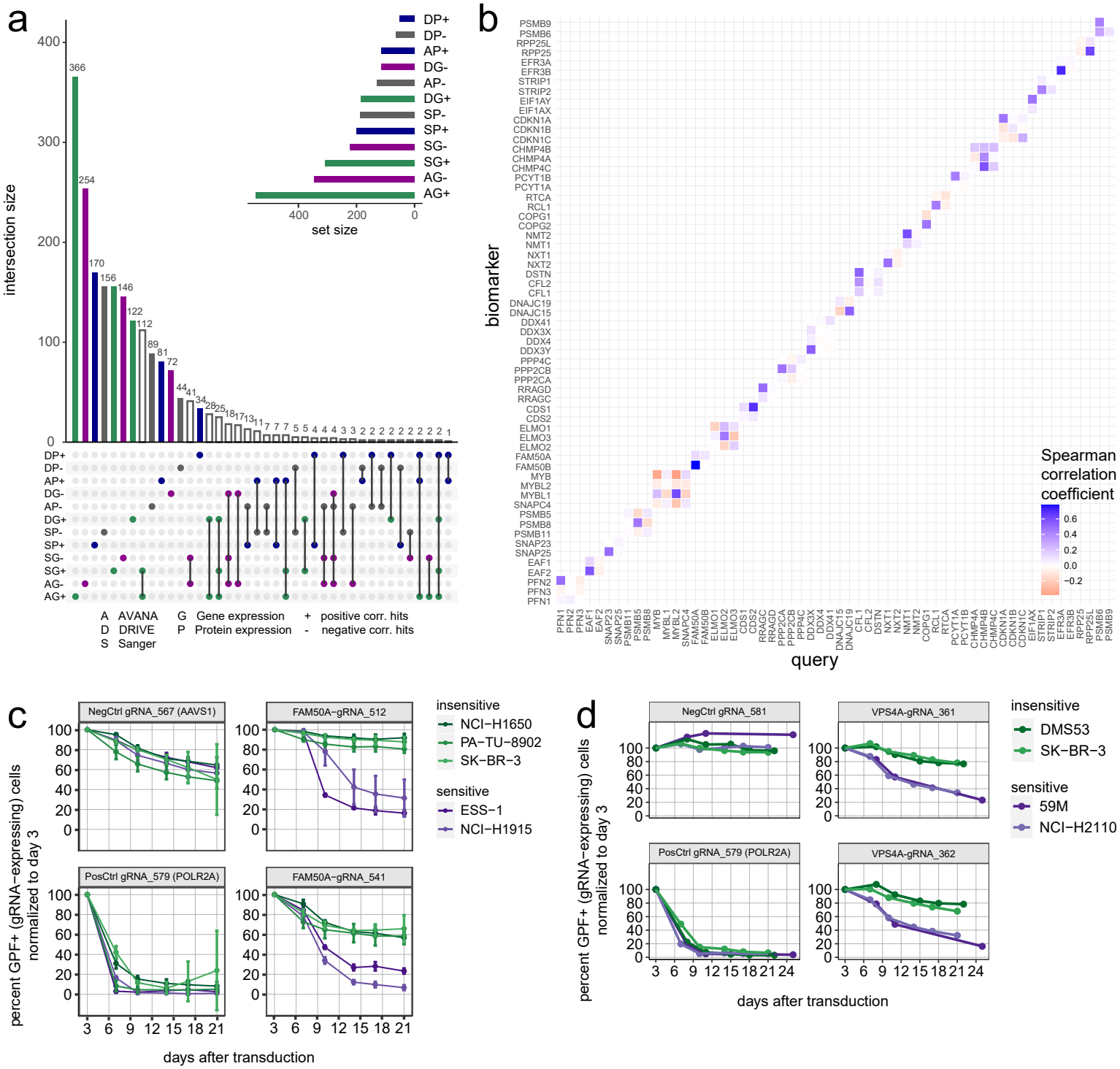
a
intersection size
set size
DP+
DP-
AP+
DG-
AP-
DG+
SP-
SP+
SG-
SG+
AG-
AG+
A AVANA
D DRIVE
S Sanger
G Gene expression
P Protein expression
+ positive corr. hits
- negative corr. hits
b
biomarker
query
Spearman correlation coefficient
c
NegCtrl gRNA_567 (AAVS1)
FAM50A-gRNA_512
PosCtrl gRNA_579 (POLR2A)
FAM50A-gRNA_541
percent GPF+ (gRNA-expressing) cells normalized to day 3
days after transduction
insensitive
NCI-H1650
PA-TU-8902
SK-BR-3
sensitive
ESS-1
NCI-H1915
d
NegCtrl gRNA_581
VPS4A-gRNA_361
PosCtrl gRNA_579 (POLR2A)
VPS4A-gRNA_362
percent GPF+ (gRNA-expressing) cells normalized to day 3
days after transduction
insensitive
DMS53
SK-BR-3
sensitive
59M
NCI-H2110

Figure 3

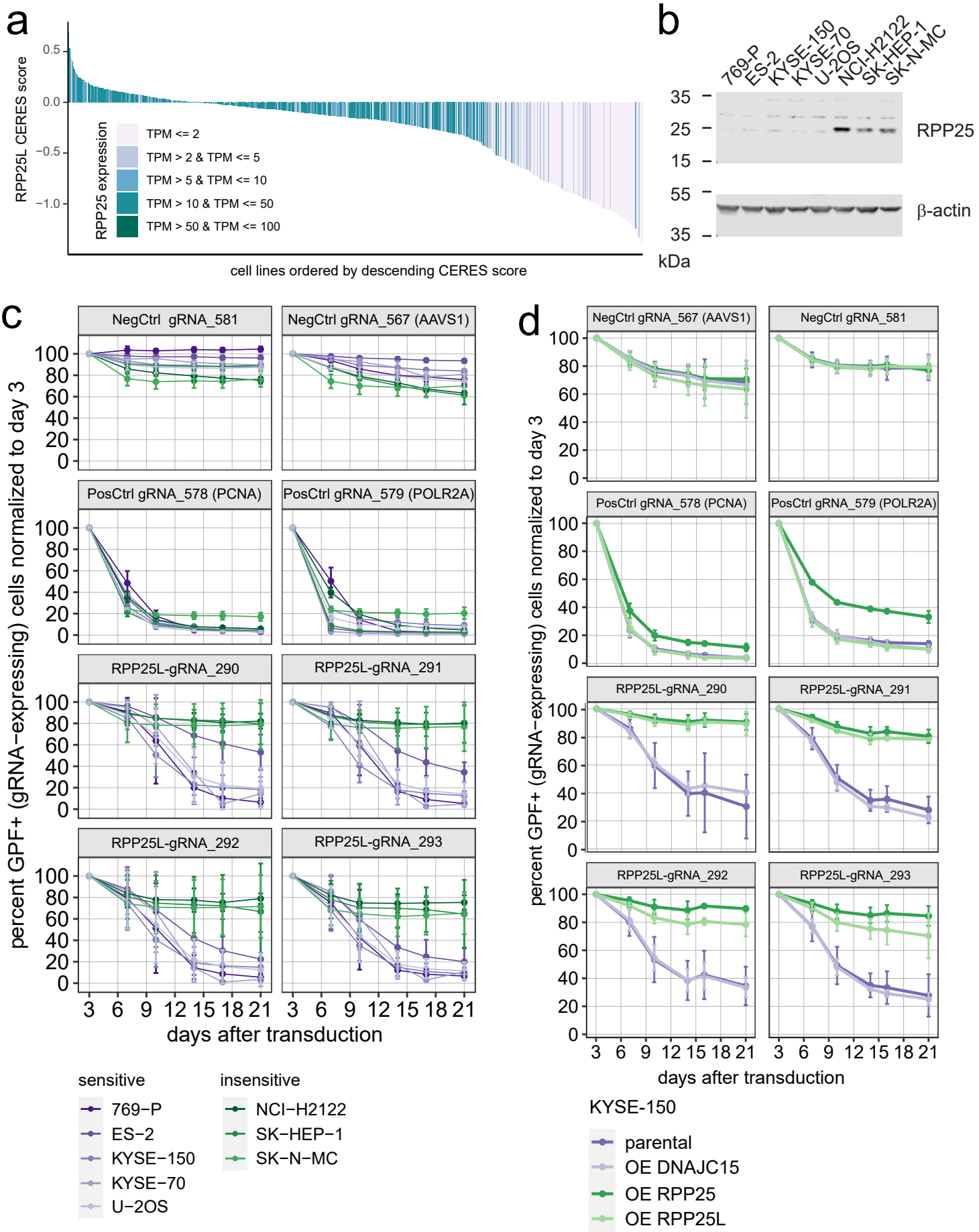
a
RPP25L CERES score
0.5
0.0
−0.5
−1.0
RPP25 expression
TPM <= 2
TPM > 2 & TPM <= 5
TPM > 5 & TPM <= 10
TPM > 10 & TPM <= 50
TPM > 50 & TPM <= 100
cell lines ordered by descending CERES score
b
769-P
ES-2
KYSE-150
KYSE-70
U-2OS
NCI-H2122
SK-HEP-1
SK-N-MC
35
25
15
55
35
kDa
RPP25
β-actin
c
NegCtrl gRNA_581
NegCtrl gRNA_567 (AAVS1)
PosCtrl gRNA_578 (PCNA)
PosCtrl gRNA_579 (POLR2A)
RPP25L-gRNA_290
RPP25L-gRNA_291
RPP25L-gRNA_292
RPP25L-gRNA_293
percent GPF+ (gRNA−expressing) cells normalized to day 3
days after transduction
sensitive
769−P
ES−2
KYSE−150
KYSE−70
U−2OS
insensitive
NCI−H2122
SK−HEP−1
SK−N−MC
d
NegCtrl gRNA_567 (AAVS1)
NegCtrl gRNA_581
PosCtrl gRNA_578 (PCNA)
PosCtrl gRNA_579 (POLR2A)
RPP25L-gRNA_290
RPP25L-gRNA_291
RPP25L-gRNA_292
RPP25L-gRNA_293
percent GPF+ (gRNA−expressing) cells normalized to day 3
days after transduction
KYSE-150
parental
OE DNAJC15
OE RPP25
OE RPP25L

Figure 4

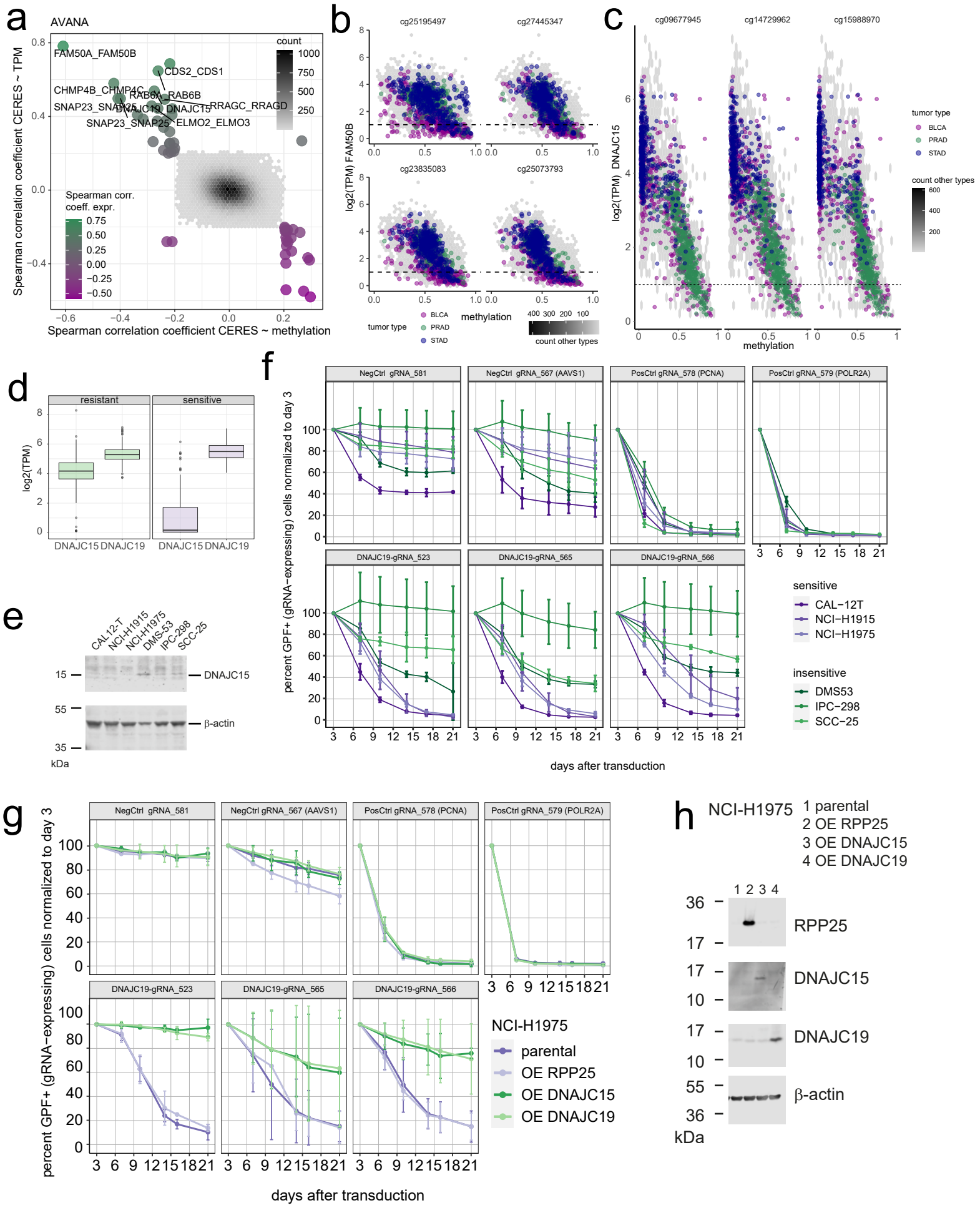
a
AVANA
FAM50A_FAM50B
CDS2_CDS1
CHMP4B_CHMP4C
RAB6A_RAB6B
SNAP23_SNAP25
DNAJC19_DNAJC15
RRAGC_RRAGD
SNAP23_SNAP25_ELMO2_ELMO3
count
Spearman corr. coeff. expr.
Spearman correlation coefficient CERES ~ TPM
Spearman correlation coefficient CERES ~ methylation
b
cg25195497
cg27445347
cg23835083
cg25073793
log2(TPM) FAM50B
methylation
tumor type
BLCA
PRAD
STAD
count other types
c
cg09677945
cg14729962
cg15988970
log2(TPM) DNAJC15
methylation
tumor type
count other types
d
resistant
sensitive
log2(TPM)
DNAJC15 DNAJC19 DNAJC15 DNAJC19
e
CAL-12-T
NCI-H1915
NCI-H1975
DMS-53
IPC-298
SCC-25
DNAJC15
β-actin
kDa
f
NegCtrl gRNA_581
NegCtrl gRNA_567 (AAVS1)
PosCtrl gRNA_578 (PCNA)
PosCtrl gRNA_579 (POLR2A)
DNAJC19-gRNA_523
DNAJC19-gRNA_565
DNAJC19-gRNA_566
percent GPF+ (gRNA−expressing) cells normalized to day 3
days after transduction
sensitive
CAL−12T
NCI−H1915
NCI−H1975
insensitive
DMS53
IPC−298
SCC−25
g
NegCtrl gRNA_581
NegCtrl gRNA_567 (AAVS1)
PosCtrl gRNA_578 (PCNA)
PosCtrl gRNA_579 (POLR2A)
DNAJC19-gRNA_523
DNAJC19-gRNA_565
DNAJC19-gRNA_566
percent GPF+ (gRNA−expressing) cells normalized to day 3
days after transduction
NCI-H1975
parental
OE RPP25
OE DNAJC15
OE DNAJC19
h
NCI-H1975
1 parental
2 OE RPP25
3 OE DNAJC15
4 OE DNAJC19
1 2 3 4
RPP25
DNAJC15
DNAJC19
β-actin
kDa

Figure 5

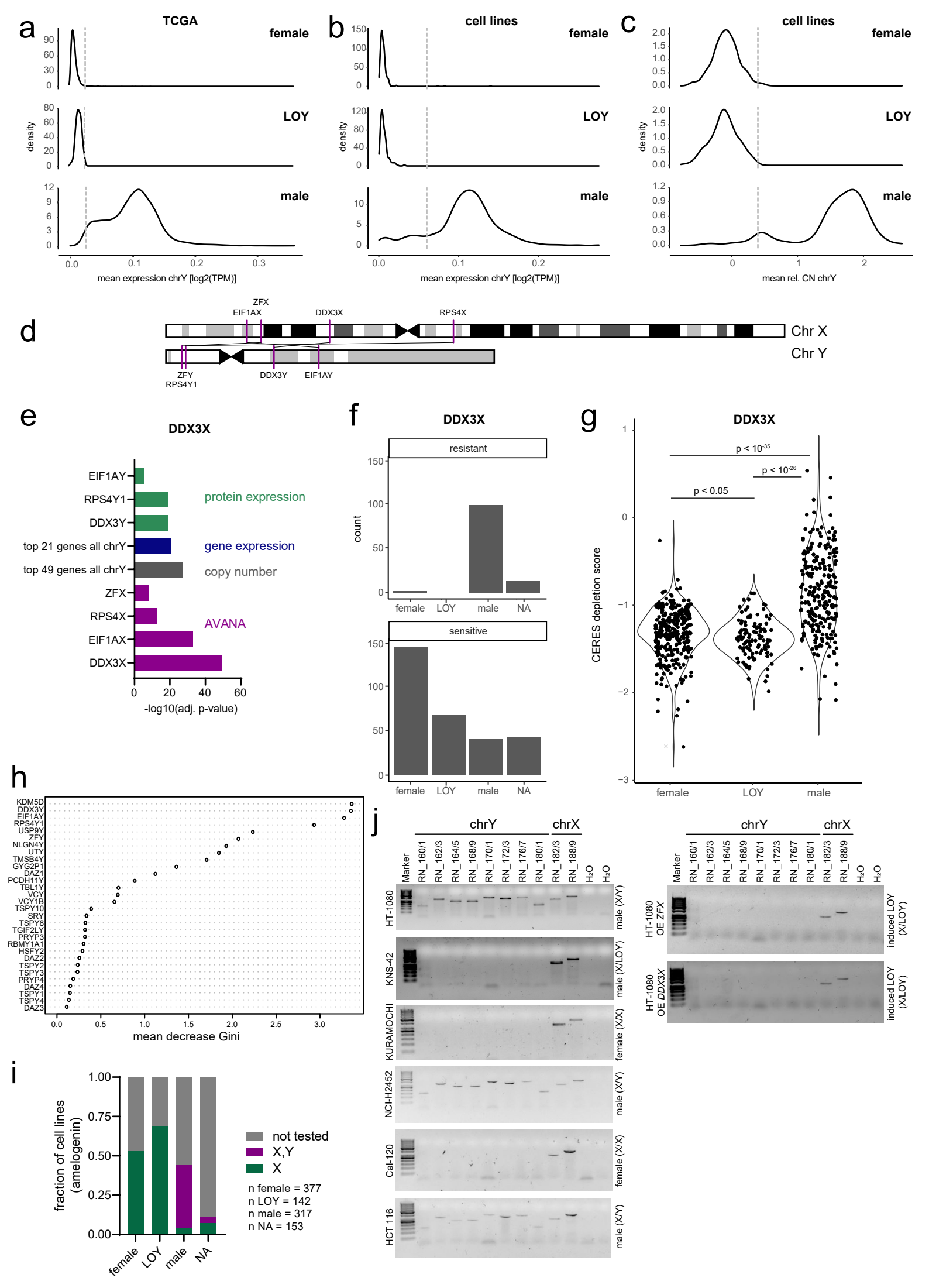
a
TCGA
female
LOY
male
density
mean expression chrY [log2(TPM)]
b
cell lines
female
LOY
male
density
mean expression chrY [log2(TPM)]
c
cell lines
female
LOY
male
density
mean rel. CN chrY
d
ZFX
EIF1AX
DDX3X
RPS4X
Chr X
Chr Y
ZFY
RPS4Y1
DDX3Y
EIF1AY
e
DDX3X
EIF1AY
RPS4Y1
DDX3Y
top 21 genes all chrY
top 49 genes all chrY
ZFX
RPS4X
EIF1AX
DDX3X
protein expression
gene expression
copy number
AVANA
-log10(adj. p-value)
f
DDX3X
resistant
sensitive
count
female
LOY
male
NA
g
DDX3X
p < 10^-35
p < 10^-26
p < 0.05
CERES depletion score
female
LOY
male
h
KDM5D
DDX3Y
EIF1AY
RPS4Y1
USP9Y
ZFY
NLGN4Y
UTY
TMSB4Y
GYG2P1
DAZ1
PCDH11Y
TBL1Y
VCY
VCY1B
TSPY10
SRY
TSPY8
TGIF2LY
PRYP3
RBMY1A1
HSFY2
DAZ2
TSPY2
TSPY3
PRYP4
DAZ4
TSPY1
TSPY4
DAZ3
mean decrease Gini
i
fraction of cell lines (amelogenin)
not tested
X,Y
X
n female = 377
n LOY = 142
n male = 317
n NA = 153
female
LOY
male
NA
j
chrY
chrX
Marker
RN_160/1
RN_162/3
RN_164/5
RN_168/9
RN_170/1
RN_172/3
RN_176/7
RN_180/1
RN_182/3
RN_188/9
H2O
H2O
HT-1080
KNS-42
KURAMOCHI
NCI-H2452
Cal-120
HCT 116
male (X/Y)
male (X/LOY)
female (X/X)
male (X/Y)
female (X/X)
male (X/Y)
HT-1080 OE ZFX
HT-1080 OE DDX3X
induced LOY (X/LOY)
induced LOY (X/LOY)

Figure 6

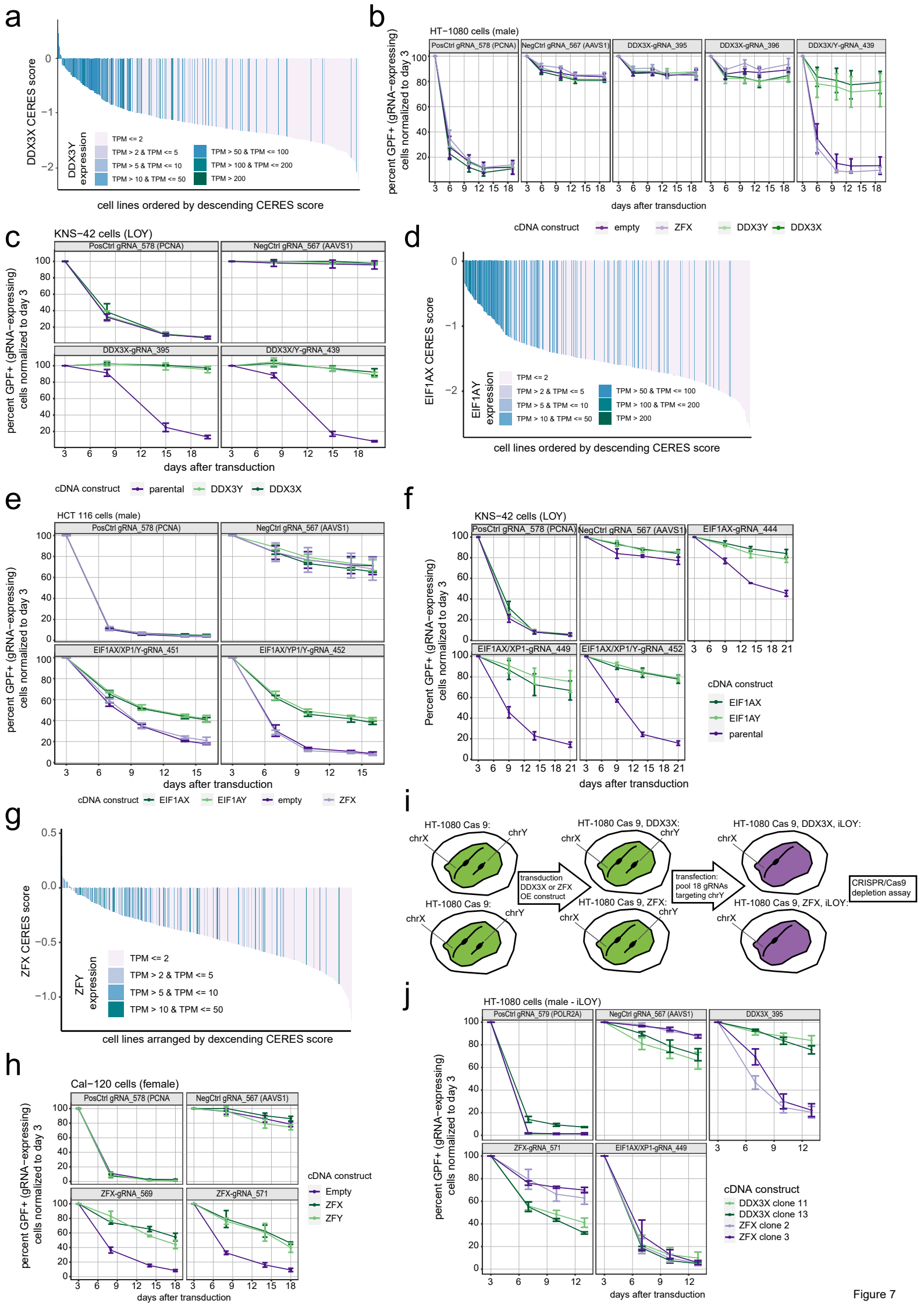
a
DDX3X CERES score
DDX3Y expression
TPM <= 2
TPM > 2 & TPM <= 5
TPM > 5 & TPM <= 10
TPM > 10 & TPM <= 50
TPM > 50 & TPM <= 100
TPM > 100 & TPM <= 200
TPM > 200
cell lines ordered by descending CERES score
b
HT−1080 cells (male)
PosCtrl gRNA_578 (PCNA)
NegCtrl gRNA_567 (AAVS1)
DDX3X-gRNA_395
DDX3X-gRNA_396
DDX3X/Y-gRNA_439
percent GPF+ (gRNA−expressing) cells normalized to day 3
days after transduction
cDNA construct
empty
ZFX
DDX3Y
DDX3X
c
KNS−42 cells (LOY)
PosCtrl gRNA_578 (PCNA)
NegCtrl gRNA_567 (AAVS1)
DDX3X-gRNA_395
DDX3X/Y-gRNA_439
percent GPF+ (gRNA−expressing) cells normalized to day 3
days after transduction
cDNA construct
parental
DDX3Y
DDX3X
d
EIF1AX CERES score
EIF1AY expression
TPM <= 2
TPM > 2 & TPM <= 5
TPM > 5 & TPM <= 10
TPM > 10 & TPM <= 50
TPM > 50 & TPM <= 100
TPM > 100 & TPM <= 200
TPM > 200
cell lines ordered by descending CERES score
e
HCT 116 cells (male)
PosCtrl gRNA_578 (PCNA)
NegCtrl gRNA_567 (AAVS1)
EIF1AX/XP1/Y-gRNA_451
EIF1AX/YP1/Y-gRNA_452
percent GPF+ (gRNA−expressing) cells normalized to day 3
days after transduction
cDNA construct
EIF1AX
EIF1AY
empty
ZFX
f
KNS−42 cells (LOY)
PosCtrl gRNA_578 (PCNA)
NegCtrl gRNA_567 (AAVS1)
EIF1AX-gRNA_444
EIF1AX/XP1-gRNA_449
EIF1AX/XP1/Y-gRNA_452
Percent GPF+ (gRNA−expressing) cells normalized to day 3
days after transduction
cDNA construct
EIF1AX
EIF1AY
parental
g
ZFX CERES score
ZFY expression
TPM <= 2
TPM > 2 & TPM <= 5
TPM > 5 & TPM <= 10
TPM > 10 & TPM <= 50
cell lines arranged by dexcending CERES score
i
HT-1080 Cas 9:
chrX
chrY
transduction DDX3X or ZFX OE construct
HT-1080 Cas 9, DDX3X:
HT-1080 Cas 9, ZFX:
transfection: pool 18 gRNAs targeting chrY
HT-1080 Cas 9, DDX3X, iLOY:
HT-1080 Cas 9, ZFX, iLOY:
CRISPR/Cas9 depletion assay
h
Cal−120 cells (female)
PosCtrl gRNA_578 (PCNA
NegCtrl gRNA_567 (AAVS1)
ZFX-gRNA_569
ZFX-gRNA_571
percent GPF+ (gRNA−expressing) cells normalized to day 3
days after transduction
cDNA construct
Empty
ZFX
ZFY
j
HT-1080 cells (male - iLOY)
PosCtrl gRNA_579 (POLR2A)
NegCtrl gRNA_567 (AAVS1)
DDX3X_395
ZFX-gRNA_571
EIF1AX/XP1-gRNA_449
percent GPF+ (gRNA−expressing) cells normalized to day 3
days after transduction
cDNA construct
DDX3X clone 11
DDX3X clone 13
ZFX clone 2
ZFX clone 3

Figure 7